Check for updates

Dissolved trivalent manganese in forest soils – interactions of natural organic ligands with manganese oxides

Constantin Lux, [iD] *[a] Kristian Ufer [iD] [b] and Tim Mansfeldt [iD] [a]

The presence of dissolved trivalent manganese (Mn^{3+}) in soils has been neglected largely due to its rapid disproportionation. However, natural organic ligands (NOLs) complex and stabilize Mn^{3+} by the formation of stable Mn^{3+}–NOL complexes. Our objectives were (i) to investigate the influence of NOLs on the dissolution of synthetic Mn oxides, (ii) to perform the speciation analysis of the resulting dissolved total Mn (Mn_T) pool, and (iii) to elucidate the principles governing abiotic formation of Mn^{3+}–NOL complexes. NOLs were obtained by extraction (0.001 M $CaCl_2$, 24 h) from a terrestrial forest floor Oe horizon (moder-like raw humus). In batch operations, NOLs reacted with either birnessite (containing Mn^{IV} and minor Mn^{III}) or manganite (containing solely Mn^{III}). The interaction between NOLs and Mn (hydr)oxides was investigated as a function of time (1–168 h, 7 steps), and pH (3–7, 5 steps). Mn speciation analysis was performed using a spectrophotometric protocol based on kinetic modeling. Results show that the dissolution of the Mn oxides increased with decreasing pH and increasing time. Mean proportions of Mn^{3+}–NOL complexes relative to the Mn_T pool ranged from 0 to $87 \pm 18\%$ (birnessite), and from 0 to $69 \pm 14\%$ (manganite). A pH-dependent formation of Mn^{3+}–NOL complexes was observed, highlighting pH as the critical parameter. Complex stability decreased with decreasing pH, while an influence of time was only assumed for strongly acidic conditions. Overall, Mn^{3+}–NOL complexes appeared to be metastable at pH 3–5 (birnessite) and below pH 7 (manganite). In addition, the formation of Mn^{3+}–NOL complexes was influenced by the individual properties of the Mn oxides as they were differing in their average oxidation state, point of zero charge, specific surface area and morphology and structure. These properties influence the formation mechanisms of Mn^{3+}–NOL complexes and, consequently, the Mn speciation. For example, they affect NOL adsorption rates and capacities, as well as the transformation and degradation of NOLs. We suggest (i) ligand-promoted non-reductive dissolution, (ii) ligand-promoted reductive dissolution, (iii) H^+-promoted dissolution, and (iv) ligand exchange as the four possible abiotic dissolution mechanisms for Mn release and Mn^{3+}–NOL complex formation. Following dissolution, either Mn^{3+}–NOL complexes were released, or released Mn^{2+} and Mn^{3+} may be complexed by additional NOLs with and without oxidation. We demonstrate that Mn^{3+}–NOL complexes are important, previously underestimated, constituents of the Mn_T pool in forest floor solutions and propose that they are a non-negligible component in terrestrial environments.

Environmental significance

Dissolved trivalent manganese (Mn^{3+}) participates in geochemical processes such as the decomposition of organic compounds, and thus affects carbon storage. In soils, however, this species has been neglected. It is, therefore, a valuable subject to study both quantitatively and qualitatively, in order to draw conclusions about its formation and stabilization. We investigated the influence of soil-derived natural organic ligands (NOLs) on the pH- and time-dependent dissolution of two synthetic Mn oxides. Subsequently, the speciation of the resulting total dissolved Mn pool was performed based on kinetic modeling. Our results demonstrate that terrestrial NOLs complex and stabilize Mn^{3+} as Mn^{3+}–NOL complexes. We propose that Mn^{3+}–NOL complexes are a non-negligible compound in soils, and that this species should be considered in biogeochemical modeling.

[a]Institute of Geography, Faculty of Mathematics and Natural Sciences, Department of Geosciences, University of Cologne, Albertus-Magnus-Platz, D-50923 Cologne, Germany. E-mail: Constantin.Lux@uni-koeln.de

[b]Federal Institute for Geosciences and Natural Resources, Stilleweg 2, D-30655 Hannover, Germany

1 Introduction

Manganese (Mn) is a versatile and ubiquitous element. As a product of weathering, Mn accumulates in global surface soils at concentrations ranging from <7 to >9000 mg kg^{-1} with mean

This journal is © The Royal Society of Chemistry 2025

Environ. Sci.: Processes Impacts, 2025, **27**, 2875–2893 | 2875

values between 270 and 530 mg kg^{-1}.[1] Its oxidation states range from -3 to $+7$.[2] In soils, the oxidation states $+2$, $+3$ and $+4$ dominate.[3]

Dissolved divalent Mn (Mn^{2+}) has been assumed to be predominant in aquatic environments, while dissolved trivalent Mn (Mn^{3+}) was considered unstable due to its rapid disproportionation.[4,5] However, various studies have shown that natural organic ligands (NOLs) complex and stabilize Mn^{3+} in marine and estuarine environments, water treatment works, and acidic forest floor solutions as well as soil solutions.[6–14] Analyses of the binding strengths between Mn^{3+} and organic model ligands allow further discrimination between weakly (Mn^{3+}–NOL$_{weak}$) and strongly bound Mn^{3+} (Mn^{3+}–NOL$_{strong}$) complexes.[10] Despite the evidence presented so far for its occurrence and dynamics, the formation, persistence, and reactivity of Mn^{3+}–NOL complexes in soils remain largely unexplored. The geochemical behavior of Mn is highly dependent on parameters such as pH and redox potential (E_H),[15] as well as the variability of soil composition, e.g., with respect to Mn oxides.[3]

More than 15 known Mn (oxyhydr)oxide minerals exist,[16,17] and they are widespread in soils. The $Mn^{III/IV}$ (oxyhydr)oxides play the largest role in terms of precipitation/dissolution processes, and Mn bioavailability.[18,19] Birnessite (δ–$Mn^{III/IV}O_2$) is a mixed-valence $Mn^{III/IV}$ oxide classified as a phyllomanganate.[20] It is one of the most abundant Mn oxides in the clay-size fraction (<2 µm) of soils.[21] Due to its high oxidation potential, birnessite oxidizes a wide range of natural organic and inorganic compounds.[22] Manganite (γ–$Mn^{III}O(OH)$) is the most abundant and stable natural polymorph of Mn oxy(hydroxide) ($MnO(OH)$) minerals.[17] We selected these two Mn oxides because of their ubiquity in natural environments and their varying physico-chemical properties. These properties include the average oxidation state (AOS), the point of zero charge (PZC), the specific surface area (SSA), and the E_H, as well as the minerals' morphology and structure.

Dissolved organic matter (DOM) is a complex pool of NOLs with various functional groups, e.g., carboxyl (R–COOH) and phenolic (R–OH) groups, and metal-binding affinities.[23] Low molecular weight organic acids (e.g., citric, oxalic or acetic acid) have carboxyl groups that bind Mn^{3+}.[24–27] Phenolic compounds, such as catechol or 2,3-dihydroxybenzoic acid, are known to form Mn^{3+}–NOL complexes.[10] In addition, amino acids and peptides (e.g., siderophores) provide suitable binding sites for Mn^{3+}.[28,29] NOLs are the key component because stable Mn^{3+} can only be formed in the presence of ligands.[30] Nevertheless, the molecular complexity of DOM makes it challenging to predict the formation of Mn^{3+}–NOL complexes.

In soils, the principle mechanisms for Mn release[3] are (i) proton (H$^+$)-promoted dissolution,[31] (ii) biological reduction (dissimilatory reductive dissolution),[32–34] (iii) abiotic reduction (reductive dissolution), and (iv) ligand-promoted dissolution of Mn oxides.[26]

In this study, the examined abiotic mechanisms for Mn oxide dissolution are defined as (i) proton (H$^+$)-promoted dissolution ($Mn^{IV}O_2 + 4H^+ + 2e^- \rightarrow Mn^{2+} + 2H_2O$), (ii) ligand-promoted reductive dissolution (e.g., $Mn^{IV} + NOL + 2e^- \rightarrow$ $Mn^{2+} + NOL_{ox}$), (iii) ligand-promoted non-reductive dissolution ($Mn^{III} + NOL \rightarrow Mn^{3+}$–NOL), and (iv) ligand exchange (Mn^{III}–OH + NOL$^- \rightarrow Mn^{III}$–NOL + OH$^- \rightarrow Mn^{3+} + NOL \rightarrow Mn^{3+}$–NOL). Because H$^+$-promoted dissolution of both Mn oxides begins at pH ≤ 5, background dissolution rates were quantified in this study in the absence of NOLs to determine NOL-induced dissolution. The gradual H$^+$-promoted release of Mn^{2+} is assumed to occur in parallel in the presence of NOLs. Looking at ligand-promoted reductive dissolution, if the NOL has reductive properties, surface-bound Mn^{IV} and Mn^{III} are converted to Mn^{3+} and Mn^{2+}. These reduced Mn species may be complexed by the same NOL or by additional NOLs, forming either Mn^{3+}–NOL or more soluble Mn^{2+}–NOL complexes,[26] with or without subsequent oxidation. The formation rate of Mn^{3+}–NOL complexes by abiotic oxidation rate is strongly dependent to the pH of the solution and the properties and concentrations of NOLs.[30] Alternatively, after adsorption onto the surface of the Mn oxides, NOLs may non-reductively detach surface-bound Mn^{III} as Mn^{3+}–NOL complexes. We assume that these mechanisms affect the formation of Mn^{3+}–NOL complexes.

Various studies have investigated the interactions between Mn oxides and NOLs including model ligands, focusing on (i) H$^+$- and ligand-promoted reductive dissolution of Mn oxides,[26,28,29,31,35–37] or (ii) oxidative degradation of organic pollutants.[38] However, a quantitative speciation analysis of the resulting total dissolved Mn (Mn_T) pool is absent from the literature.

Our main objectives were (i) to determine Mn_T solution speciation, including Mn^{2+} (sum of Mn^{2+} and Mn^{2+}–NOL complexes) and Mn^{3+}–NOL complex (sum of Mn^{3+}–NOL$_{weak}$ and Mn^{3+}–NOL$_{strong}$) concentrations, and (ii) to elucidate the principles of the Mn^{3+}–NOL complex formation as a result of the abiotic dissolution of Mn oxides. A thorough understanding of the Mn^{3+}–NOL complex formation in soil solutions is highly relevant, as the strong oxidant Mn^{3+} affects the decomposition of organic matter (OM) and the associated release of carbon dioxide (CO_2).[39–44] Furthermore, it contributes to the degradation of organic pollutants,[45,46] such as methylmercury,[38] and is redox-active in water treatment works.[6]

In order to address these issues, a spectrophotometric method (porphyrin method), employing $\alpha,\beta,\gamma,\delta$-tetrakis(4-carboxyphenyl)porphine (T(4-CP)P), was applied.[7] This analysis enables direct qualification and quantification of the dissolved Mn species by kinetic modeling. The principal mechanism behind the porphyrin method is a metal substitution reaction. Divalent cadmium (Cd^{2+}) bound to the porphyrin (Cd^{2+}–T(4-CP)P) is replaced by free or NOL-bound Mn^{2+} and Mn^{3+} present in the sample. Thus, the method allows differentiation of the dissolved Mn_T pool based on ligand binding affinities and strengths to Mn^{2+} and Mn^{3+}.[7,8,10] From this, the proportions of Mn^{2+}, Mn^{3+}–NOL$_{weak}$ complexes and Mn^{3+}–NOL$_{strong}$ complexes are derived by fitting the experimental data using kinetic modeling equations. Two series of batch operations were conducted under oxidizing conditions to evaluate the influences of pH and time on NOL–Mn oxide interactions. A normalized, 'native' Mn and (trace) metal cation free, DOM-stock solution from an acidic spruce site was extracted and

2876 | Environ. Sci.: Processes Impacts, 2025, **27**, 2875–2893

This journal is © The Royal Society of Chemistry 2025

freshly prepared for each batch experiment. Subsequently, the extract was reacted with either birnessite or manganite. The synthesized Mn oxides offer the possibility of studying different dissolution mechanisms that can be accessed by Mn speciation analysis.

2 Materials and methods

2.1 Sampling of the forest floor

Forest floor samples were collected at the permanent environmental monitoring station #101 at Idar-Oberstein (49° 44′33.38″N, 7°11′47.61″E), Rhineland-Palatinate, Germany, which is managed by the federal state authority Research Institute for Forest Ecology and Forestry of the state of Rhineland-Palatinate in Trippstadt.[47] The soil is classified as a Dystric Cambisol[48] and covered by stands of spruce (*Picea abies* (L.) H. Karst.).

From the Oe horizon (+5–+9 cm),[49] characterized as moder-like raw humus,[50] about 5 kg of fresh material was obtained over an area of 15 m^2. In the laboratory, the material was sieved to <2 mm and stored in polypropylene (PP) bags in the dark at 4 °C to minimize changes in composition.[51] A subsample was dried at 60 °C and finely ground in an agate ball mill (PM 400, Retsch, Haan, Germany).

2.2 Experimental methods

2.2.1 Forest floor. The pH of the Oe horizon was examined potentiometrically in a 0.01 M calcium chloride (CaCl$_2$) solution and ultrapure water using a glass electrode (SenTIX 81, WTW, Weilheim, Germany). A conductivity electrode (SevenEasy, Mettler Toledo, Giessen, Germany) was used to measure electrical conductivity (EC) in a suspension of the Oe material and deionized water (1 : 5 w : v). Total carbon (TC) and nitrogen (N) were determined in duplicate by dry combustion of ground samples using a CNS analyzer (Vario EL cube, Elementar, Hanau, Germany) equipped with a thermal conductivity conductor.

2.2.2 Extraction of the DOM-stock solution. A fresh DOM-stock solution (3.75 ± 0.17 mmol C L^{-1}) was obtained for each batch operation by 0.001 M CaCl$_2$ extraction of the Oe horizon. The extraction was modified on the basis of CaCl$_2$ extractions described in the literature, which employed various methodological approaches.[52–54] 40 g of forest floor material and 200 mL of a 0.001 M CaCl$_2$ solution (1 : 5 w : v) were put in a 500 mL amber glass flask. The glass was then shaken constantly at 9 rpm on an overhead shaker (Reax 20/21, Heidolph Instruments, Schwabach, Germany) for 24 h at 22 ± 1 °C. Centrifugation at 4000 g (Rotina 420 R, Hettich, Kirchlengern, Germany) for 10 min was followed by filtration through a <2 μm ashless blue ribbon filter (589/3, Whatman®, Maidstone, United Kingdom). Next, the extract was passed through a 0.2 μm filter (cellulose acetate, Sartorius, Göttingen, Germany) using acid-cleaned filtration units (polycarbonate, Sartorius, Göttingen, Germany). In order to remove 'native' Mn and (trace) metal cations from the DOM-stock solution, it was passed four times through a cation exchange column (2.5 × 50 cm) filled with an acidic cation exchange resin (Dowex® 50W-X8 cation exchange resin, mesh 16–50, Dow Chemical, Michigan, USA). A flow rate of 13 mL min^{-1} was applied following the protocol presented by Strobel *et al.* (2001).[55] Subsequently, the H$^+$-saturated extract was refiltered through 0.2 μm cellulose acetate filters in order to remove potential residues of the cation exchange resin. The removal of 'native' Mn and (trace) metal cations was checked by inductively coupled plasma optical emission spectrometry (ICP OES). Sodium azide (NaN$_3$) was added at a concentration of 0.01 M to the DOM-stock solution in order to suppress biological activities.[56]

To determine the total dissolved organic C (DOC) concentration in the DOM-stock solution, a sample volume of 100 μL was injected into a small glass tube and subjected to high-temperature catalytic oxidation to CO$_2$ at 850 °C. The DOC content was quantified using a non-dispersive infrared TOC analyzer (Dimatoc 2000, Dimatec, Essen, Germany). All samples were analyzed in triplicate.

2.2.3 Characterization of the DOM-stock solution. Excitation-emission matrix (EEM) spectroscopy was applied on the DOM-stock solution using a fluorescence spectrometer (FLS 980, Edinburgh Instruments, Livingston, United Kingdom) equipped with a 450 W xenon lamp as the excitation source and a photomultiplier (PMT) detector (R928P, Hamamatsu Photonics, Shizuoka, Japan) at the Department of Chemistry, University of Cologne. Excitation (Ex) wavelengths (200–500 nm, 10 nm steps) and emission (Em) wavelengths (250–700 nm, 1 nm steps) were recorded in a 1 cm quartz cuvette at 22 ± 1 °C. The slits of excitation and emission were set to 2.5 nm and 3.0 nm, respectively. Before the EEM recording, all samples were checked for their absorbance at 254 nm and were diluted with ultrapure water (18.2 MΩ cm) to an absorbance of <0.3 A in order to avoid inner filter effects.[57] The dilution factor was considered in the further calculations. Subtracting the ultrapure water blank spectrum eliminated Raman scattering.[58] In order to further characterize the initial DOM pool, three indices were calculated according to literature: (i) the fluorescence index (FI),[59] (ii) the humification index (HIX),[57,60] and (iii) the biological index (BIX)[61] (see SI). Additionally, four major fluorescent DOM (FDOM) component peaks (B, T, A, C) characterizing terrestrial FDOM were determined. Peak B is at $E_x/E_m =$ 275/310 nm and includes tyrosine-like and protein-like signals; peak T, at $E_x/E_m =$ 275/340 nm, indicates tryptophan-like and protein-like signals. Peak A is at $E_x/E_m =$ 260/380–460 nm and peak C is at $E_x/E_m =$ 350/420–480 nm – both mark humic-like FDOM components.[62] Calculating the FDOM data was done in R (version 4.2.2)[63] using RStudio (version 2022.12.0)[64] and the package *staRdom* (version 1.1.25).[65]

2.3 Preparation of Mn oxides

The preparation of the birnessite followed the protocol by Rabenhorst and Persing (2017).[66] Manganite synthesis was performed according to the method of Giovanoli and Leuenberger (1969),[67] modified after Lee *et al.* (1980).[68] Detailed descriptions of the syntheses are provided in the SI.

This journal is © The Royal Society of Chemistry 2025

Environ. Sci.: Processes Impacts, 2025, **27**, 2875–2893 | **2877**

2.3.1 Characterization of Mn oxides. The synthesized Mn oxides were analyzed by X-ray powder diffraction (XRD), scanning electron microscopy (SEM) and the Brunauer–Emmett–Teller method (BET) at the Federal Institute for Geosciences and Natural Resources (BGR, Hannover, Germany). Additionally, attenuated total reflection Fourier-transform infrared spectroscopy (ATR FT-IR) was performed at the Department of Chemistry, University of Cologne (Cologne, Germany). The AOS and the PZC were determined at the Institute of Geography, University of Cologne. More detailed information can be found in the SI.

2.4 Batch experiments

Batch operations were chosen in order to investigate the effects of pH (3–7, 5 steps) and time (1–168 h, 7 steps). Initially, 20 ± 0.1 mg of Mn oxide was weighed into a 50 mL PP centrifuge tube (Sarstedt, Nürnbrecht, Germany) and covered in aluminum foil to block ambient light. Subsequently, a 30 mL aliquot of the freshly prepared DOM-stock solution (3.75 ± 0.17 mmol C L^{-1}) was adjusted with 10 M HNO$_3$ ($\leq$100 µL) or 10 M NaOH ($\leq$100 µL) based on preliminary experiments to maintain the desired pH, then added to the tube. The suspension was shaken on a horizontal shaker (GFL-3006, Lauda, Lauda-Königshofen, Germany) at 200 rpm for a predefined batch operation time at constant atmospheric conditions ($T = 20 \pm 0.1$ °C, $p = 0.1013$ MPa). The suspension was then immediately passed through a 0.2 µm cellulose acetate filter. After filtration, pH (827 pH Lab, Metrohm, Herisau, Switzerland) and EC (SevenEasy™, Mettler-Toledo, Columbus, USA) values were recorded. Experimental samples (in triplicate) were prepared for Mn speciation analysis (in triplicate for each sample), subsequent DOM measurements by UV/Vis spectroscopy (in duplicate) and determination of the DOC concentrations (in triplicate). The H$^+$-promoted background dissolution rates were separately determined in the absence of NOLs at pH 3, 4, and 5. Total Mn concentrations in this experiment were quantified by ICP OES.

2.5 Mn speciation analysis by kinetic modeling

Dissolved Mn speciation analysis was performed using the spectrophotometric porphyrin method, following the protocols outlined in Madison et al. (2011)[7] and Oldham et al. (2015).[10] The extended protocol for acidic forest soil solutions and soil solutions was applied as described in Lux and Mansfeldt (2023).[9] In summary, the spectrophotometric analyses included the determination of Mn^{2+}, Mn^{3+}–NOL$_{weak}$ complexes, Mn^{3+}–NOL$_{strong}$ complexes, and Mn$_T$ based on kinetic modeling. They were conducted at a specific Soret band (468 nm) using (T(4-CP)P). All absorbance measurements were performed on a Lambda 25™ spectrophotometer (PerkinElmer®, Rodgau, Germany) using a 1 cm pathlength glass cuvette with 3 mL of total volume. Prior to the analyses, the absorption coefficient ($\varepsilon = 95\,340$ M^{-1} cm^{-1}) for the Mn^{3+}–T(4-CP)P complex was determined using manganese chloride tetrahydrate (MnCl$_2$·4H$_2$O) standards (0.1–10 µM). The concentrations of T(4-CP)P and cadmium chloride (CdCl$_2$) in the cuvettes were 24 µM each, as proposed by Madison et al. (2011).[7] The method requires a controlled pH range of 7.5–8 to facilitate the metal substitution reaction between Cd^{2+}–T(4-CP)P and Mn^{2+} or Mn^{3+}–NOL$_{weak}$ complexes. In order to maintain this pH range, a borate buffer mix was used.

The pipetting volumes of the samples were adapted to the expected Mn$_T$ concentrations in the cuvette and ranged from 50 to 2360 µL to comply with the method's detection range. Subsequently, the absorption was recorded every 5 seconds over a period of 10 minutes. The recording was stopped earlier depending on kinetics and the formation of a sufficient plateau, which indicated that the absorbance maximum was reached and the metal substitution reaction had ended.

In DOM-rich solutions, inherent coloration can interfere with the Soret band at 468 nm. Therefore, a background correction was performed.[9] The same sample quantity used in the porphyrin method was placed in a cuvette and diluted with ultrapure water to a final volume of 3 mL. Absorbance was measured against 3 mL of ultrapure water at 468 nm for the same duration as the corresponding Mn speciation analysis. The resulting background absorbance was then subtracted from the Mn absorbance measurement to correct for interference.

For each sample, a 10 mL aliquot was mixed with 10 µL of concentrated HNO$_3$ (suprapur®, 65%) for subsequent ICP OES analysis. It should be noted that acidification of humic-rich samples to a pH value <2 leads to precipitation of humic substances and thus to an underestimation of metal concentrations.[12]

As described by Madison et al. (2011),[7] the kinetic modeling approach was tested on several Mn^{2+}/Mn^{3+}–pyrophosphate mixtures with varying species concentrations. Initial Mn^{2+} and Mn^{3+} concentrations were predicted within 0.4–2% of their known values. These results suggest that the method can be a reliable tool for Mn speciation analysis. However, it must be considered that unknown environmental samples contain a diverse DOM pool and a complex solution matrix, characterizing them a as 'black box'.

The kinetic modeling of the dissolved Mn$_T$ pool was carried out as outlined in Lux and Mansfeldt (2023).[9] In order to determine the dissolved Mn$_T$ pool, two separate measurements were performed: one in the absence (non-reduced samples) and one in the presence of the strong reducing agent hydroxylamine (reduced samples). The modeling equations proposed by Madison et al. (2011)[7] were extended by introducing an additional parameter (t_0) to estimate the reaction start time, as it did not coincide with the first absorbance measurement due to manual operation [eqn (1) and (2)]. Initially, kinetic modeling of the non-reduced samples provides the concentrations of Mn^{2+} and Mn^{3+}–NOL$_{weak}$ complexes [eqn (1)], where Mn^{2+}, Mn^{3+}–NOL$_{weak}$ complexes, k_1, k_2 and t_0 are parameterized. Mn^{3+}–NOL$_{weak}$ complexes comprise NOLs with different binding affinities and strengths, which most strongly influence the reaction kinetics and thus the recorded absorbance curves. In order to clearly differentiate Mn^{3+}–NOL$_{weak}$ complexes from Mn^{2+}, the condition $k_1 \geq 3 \cdot k_2$ has to be satisfied.[14]

In the second modeling step, the concentration of Mn$_{T(hydroxylamine)}$, representing Mn^{2+} and all forms of Mn^{3+}–NOL complexes, was determined by parameterizing Mn^{2+}, k_1,

2878 | Environ. Sci.: Processes Impacts, 2025, **27**, 2875–2893

This journal is © The Royal Society of Chemistry 2025

and t_0 [eqn (2)]. The addition of the reducing agent was necessary to model the concentration of Mn^{3+}, which is methodically defined as $Mn^{3+}–NOL_{strong}$ complexes, since the ligand-bound Mn^{3+} cannot be outcompeted by T(4-CP)P.[10] The concentration of $Mn^{3+}–NOL_{strong}$ complexes was determined by calculating the difference between the reduced and the non-reduced sample [eqn (3)]. Together, the modeling equations require the estimation of eight parameters for each speciation analysis.

Five-parameter equation:

$$Mn_T = (Mn^{3+}–T(4-CP)P)_T = Mn^{2+}\cdot(1 - e^{-k_1\cdot(t-t_0)}) + Mn^{3+}–NOL_{weak}\cdot(1 - e^{-k_2\cdot(t-t_0)}) \quad (1)$$

where $Mn^{2+} = Mn^{2+}$ concentration ($\mu mol\ L^{-1}$); $Mn^{3+}–NOL_{weak} = Mn^{3+}–NOL_{weak}$ concentration ($\mu mol\ L^{-1}$); $k_1 = Mn^{2+}$ rate constant (s^{-1}); $k_2 = Mn^{3+}–NOL_{weak}$ rate constant (s^{-1}); t = reaction time (s); and t_0 = reaction start (s).

Three-parameter equation:

$$Mn_{T(hydroxylamine)} = Mn^{2+}\cdot(1 - e^{-k_1\cdot(t-t_0)}) \quad (2)$$

where $Mn^{2+} = Mn^{2+}$ concentration ($\mu mol\ L^{-1}$); $k_1 = Mn^{2+}$ rate constant (s^{-1}); t = reaction time (s); and t_0 = reaction start (s).

$$Mn^{3+}–NOL_{strong} = Mn_{T(hydroxylamine)} - (Mn^{2+} + Mn^{3+}–NOL_{weak}) \quad (3)$$

An R code written in RStudio (version 2022.12.0)[63] using R (version 4.2.2)[62] and the *nlmrt* package (version 2016.3.2)[69] was executed. The initial parameter estimation [eqn (1) and (2)] was performed using the *wrapnls* method, which attempts to solve the nonlinear sum of squares problem by employing the *nlxb* algorithm and introducing predefined lower and upper limits for each parameter. Thereafter, the nonlinear least squares (nls) method based on the stats package (version 4.2.2)[63,70] was executed in order to estimate the parameters more precisely. To verify the goodness of fit to the recorded data, the root mean square error (RMSE) was determined. As reported by Johnson *et al.* (2018)[6] and by Lux and Mansfeldt (2023),[9] smaller rate constants for the $MnCl_2$ standards (reaction end in approximately 90 s) were determined in contrast to Madison *et al.* (2011),[7] and considered in the modeling process.

2.6 Characterization of DOM-stock and DOM-batch solutions

The pH- and time-dependent, qualitative and quantitative, changes of the batch DOM pool in relation to the DOM-stock solution after interaction with the Mn oxides were investigated. Prior to the experiments, the DOM-stock solution was adjusted to a DOC concentration of 3.75 ± 0.17 mmol C L^{-1} using a 0.01 M $CaCl_2$ solution as a background electrolyte. Various parameters, including the DOC concentration, the molar absorption (MA), the absorption ratio (A), the spectral slope (S), and the spectral slope ratio (S_R) were determined for reacted DOM-batch samples using a TOC analyzer and UV/Vis spectroscopy. UV/Vis spectra were collected for samples using an UV/Vis spectrometer (Lambda 25™, PerkinElmer®, Rodgau,

Germany). Scans were performed from 800 to 200 nm with a 1 nm decrement to prevent UV-induced DOM degradation. All samples were analyzed in a 1 cm pathlength cuvette against a 3 mL ultrapure water (18.2 MΩ cm) reagent blank at 20.0 ± 0.1 °C.[71] Molar absorptions at 254, 280, and 350 nm were calculated in order to elucidate the aromaticity of DOM, *e.g.*, humic substance aromaticity[71–73] and relations to molecular weight (MW).[74] The absorbance ratio A_{280}/A_{350} is reported as a well correlating parameter for both aromaticity and MW.[73] Spectral slopes were determined over the wavelength ranges 275–295 nm ($S_{275–295}$), 290–350 nm ($S_{290–350}$), and 350–400 nm ($S_{350–400}$). These are related to phototransformation of low molecular weight (LMW) material to more humic-like material as well as information about LMW material and aromaticity.[72,75,76] Finally, the S_R ($S_{275–295}/S_{350–400}$) was calculated as a proxy of DOM MW and photobleaching.[76] Calculations of the DOM parameters were performed using the R package *staRdom*.[65]

3 Results

3.1 Forest floor

The Oe horizon showed a strongly acidic pH of 3.6 ± 0.008 in 0.01 M $CaCl_2$ and 4.7 ± 0.006 in ultrapure water. An EC of 153 ± 11.2 μS cm^{-1} was determined. Elemental analysis revealed proportions of $47.0 \pm 0.8\%$ C and $1.7 \pm 0.0\%$ N resulting in a C/N ratio of 27.1 ± 0.3, indicating a moder-like raw humus.[50]

3.2 Characterization of the DOM-stock solution

The DOM-stock solution had a strongly acidic pH of 2–3 and the ICP OES analysis revealed Mn concentrations <0.182 μmol L^{-1}. DOC concentrations averaged 3.75 ± 0.17 mmol C L^{-1} after protonation by the cation exchange resin, which is similar to forest floor solutions reported in the literature.[77] A substantial loss of DOC was not observed. Further analysis by EEM spectroscopy revealed humic-like peaks (denoted as A and C), while distinct protein-like (B and T) and fulvic-like (D and E) FDOM peaks were absent (Fig. S4). An A/C peak ratio of 1.83 confirmed a blue-shifted humic-like FDOM. Additionally, calculated values for the BIX (0.400), FI (1.58), and HIX (0.966) were derived from the 3D scan.

3.3 Batch experiments

3.3.1 Total manganese concentrations. Fig. 4 shows the development of the dissolved Mn_T concentrations as a function of pH and time analyzed by ICP OES (see Tables S2 and S3). The H^+-promoted background dissolution (pH ≤ 5) of the Mn oxides was subtracted in order to determine the exclusively NOL-induced dissolution ($Mn_{T(NOL)}$).

For birnessite (Fig. 1a), the following general trends were observed: (i) a decrease in pH results in higher Mn concentrations, (ii) a longer reaction times promote an increased Mn release, and (iii) the lower the pH the lower the NOL-induced dissolution relative to the H^+-promoted dissolution. Mean $Mn_{T(NOL)}$ concentrations ranged from 0.884 ± 0.212 to 899 ± 108 μmol L^{-1} (Table S2) and peaked at pH 3 after 168 h (Fig. 1a).

This journal is © The Royal Society of Chemistry 2025

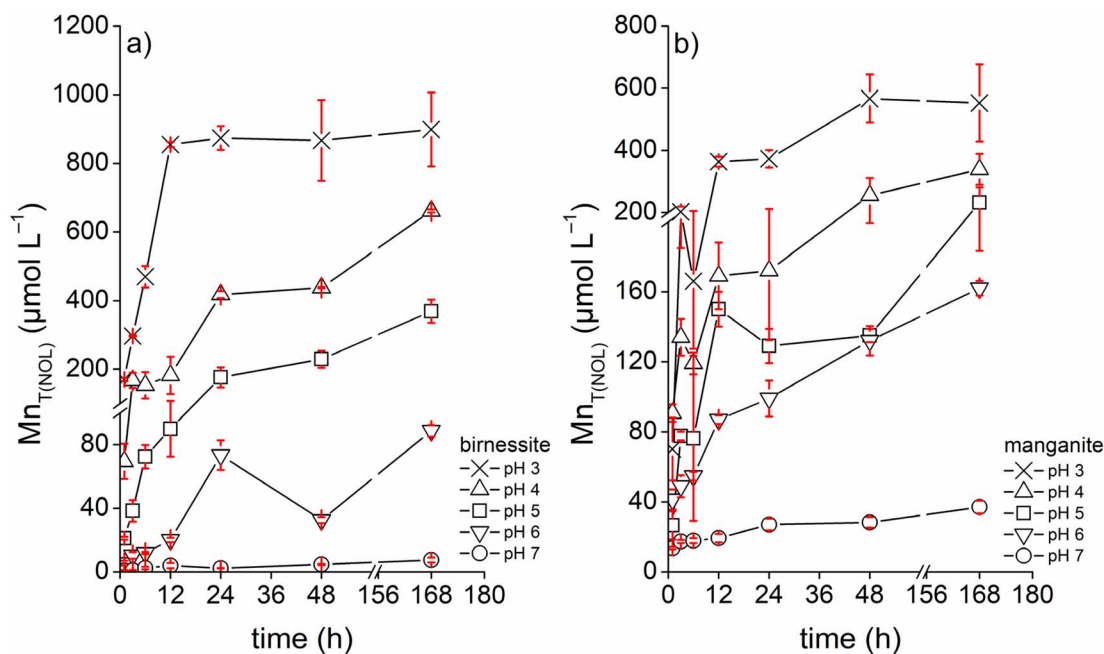*Environ. Sci.: Processes Impacts*, 2025, **27**, 2875–2893 | **2879**

Fig. 1 $Mn_{T(NOL)}$ concentrations of pH-dependent and NOL-induced Mn oxide dissolution over time for (a) birnessite, and (b) manganite. H^+-promoted background dissolution was subtracted. Each experiment was conducted in triplicate and analyzed by ICP OES. $Mn_{T(NOL)}$ = total dissolved Mn by NOL-induced dissolution; NOL = natural organic ligand.

The largest proportions of $Mn_{T(NOL)}$ (100%) were revealed at pH 6 and 7 (Table S2). By contrast, the lowest proportions were observed at pH 4 ranging between 37.8 ± 3.9 and $73.9 \pm 0.1\%$ with an overall mean of $58.5 \pm 10.7\%$ (Table S2). The highest dissolution rates were identified within the first 24 h. Prolonged batch operations revealed considerably slower dissolution kinetics.

Manganite showed similar general trends to birnessite (Fig. 1b). In comparison, the mean $Mn_{T(NOL)}$ concentrations ranged from 13.6 ± 0.675 to 567 ± 22.4 μmol L^{-1} (Table S3) and revealed an almost halved maximum concentration at pH 3 after 48 h. The highest proportions (100%) of NOL-induced dissolution were observed at pH 6 and 7 (Table S3). On the other hand, the lowest means were recorded at pH 3 ranging from 20.9 ± 4.3 to $47.1 \pm 1.1\%$ with an overall mean of $38.1 \pm 9.2\%$ (Table S3). This indicates a further significant reduction in NOL-induced dissolution under strongly acidic conditions compared to the birnessite batch experiments. Particularly noteworthy is the increased release of Mn at pH 6 and 7. Equally, the manganite batch experiments showed that increasing acidic conditions and a prolonged batch operation contributed to an increased dissolution. Looking at the dissolution kinetics, the dissolution of manganite was most rapid in the first 12 h, in particular with decreasing pH. Subsequently, the dissolution decreased sharply.

Considering the additional H^+-promoted dissolution, mean Mn_T concentrations during the birnessite batch experiments ranged from 0.884 ± 0.212 to 1418 ± 108 μmol L^{-1} (Table S2) and revealed a higher solubility of birnessite compared to manganite. The $Mn_{T(Porph)}/Mn_{T(ICP\ OES)}$ ratio for birnessite ranged from 0.87 to 1.27 with a mean of 1.03 ± 0.08 ($n = 35$, $r =$

0.996, $R^2 = 0.991$, $p < 0.001$). The manganite batch experiments revealed a narrower range of mean Mn_T concentrations (13.6 ± 0.675 to 1338 ± 77.4 μmol L^{-1}) (Table S3). For manganite, the $Mn_{T(Porph)}/Mn_{T(ICP\ OES)}$ ratio ranged from 0.85 to 1.17 with a mean of 1.02 ± 0.06 ($n = 35$, $r = 0.998$, $R^2 = 0.995$, $p < 0.001$).

The results show that NOL-induced dissolution (pH $\leq$ 5) appears to be an important process. However, the relative contribution to the overall dissolution decreased with decreasing pH, rendering H^+-promoted dissolution more effective especially during manganite batch experiments. Based on these findings, possible abiotic dissolution mechanisms are outlined in Section 4.1.

3.3.2 Kinetic modeling. Fig. 2 presents experimental data from the Mn speciation analysis of a single birnessite (non-reduced) and a single manganite (non-reduced) sample in the presence of NOL at pH 7 after 1 h. For each sample, two representative analytical measurements (A and B) are depicted in order to highlight clear differences in reaction kinetics. Kinetic modeling was conducted to fit the data including Mn^{2+} and Mn^{3+}–NOL$_{weak}$ complexes [eqn (1)]. For clarity, the modeled Mn^{3+}–NOL$_{strong}$ complexes are not shown, as weakly binding ligands primarily influence the reaction kinetics when employing the porphyrin method. Fig. 3 depicts the modeled proportions of Mn^{2+}, Mn^{3+}–NOL$_{weak}$ and Mn^{3+}–NOL$_{strong}$ complexes relative to Mn_T for both samples. Notable differences in the reaction kinetics between the Mn oxides were observed, as indicated by distinct curve shapes (Fig. 2) and substantial variations in the modeled Mn^{3+}–NOL$_{weak}$ complex proportions (Fig. 3).

In particular, the recorded curves for the NOL–birnessite interactions appear flattened (Fig. 2a) compared to those for manganite (Fig. 2b), indicating slower reaction kinetics. Kinetic
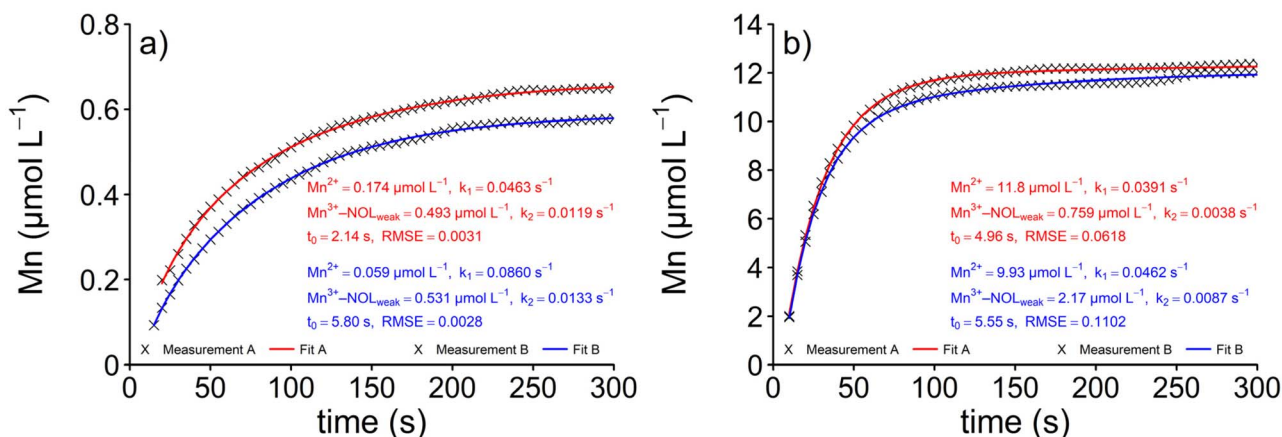
2880 | Environ. Sci.: Processes Impacts, 2025, **27**, 2875–2893

This journal is © The Royal Society of Chemistry 2025

Fig. 2 Kinetic modeling of (a) a single birnessite (non-reduced) and (b) a single manganite sample (non-reduced) at pH 7 after 1 h. The analysis of the non-reduced sample represents the Mn speciation analysis without the hydroxylamine treatment. The modeling includes complexes of Mn^{2+} and $Mn^{3+}-NOL_{weak}$ (Tables S2 and S3), excluding $Mn^{3+}-NOL_{strong}$ complexes. Two analytical measurements (A and B) are demonstrated for each sample, along with the corresponding fits: measurement A (black crosses) with fit A (red line), and measurement B (black crosses) with fit B (blue line)). NOL = natural organic ligand; $Mn^{3+}-NOL_{weak}$ = weakly bound Mn^{3+}; $Mn^{3+}-NOL_{strong}$ = strongly bound Mn^{3+}.
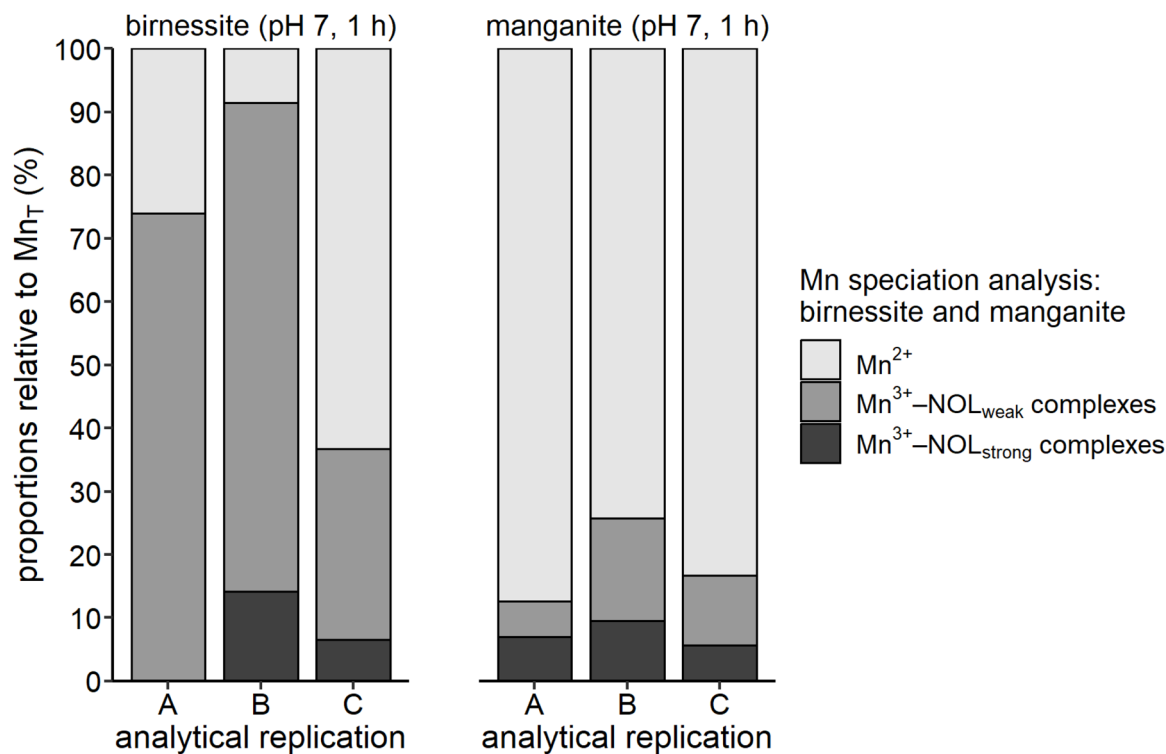

Fig. 3 Mn speciation analysis in triplicate (A–C) of a single birnessite and manganite sample at pH 7 after 1 h. Mn_T = total dissolved Mn; $Mn^{3+}-NOL_{weak}$ = weakly bound Mn^{3+}; $Mn^{3+}-NOL_{strong}$ = strongly bound Mn^{3+}.

modeling of the analytical replicates A and B revealed sample-specific dominant proportions of $Mn^{3+}-NOL_{weak}$ complexes, accounting for 73.9 and 77.2% relative to Mn_T (Fig. 3). Proportions of Mn^{2+} contributed 26.1 and 8.6%, while $Mn^{3+}-NOL_{strong}$ complexes accounted for 0 and 14.2%, respectively (Fig. 3).

Manganite, in contrast, exhibited faster reaction kinetics (Fig. 2b), as the curves plateaued more quickly. After 1 h, only minor traces of $Mn^{3+}-NOL_{weak}$ complexes (16.2 and 5.6%) were

detected, while Mn^{2+} was the dominant species (74.3 and 86.9%) (Fig. 3). The sample-specific proportions of $Mn^{3+}-NOL_{strong}$ complexes were 8.5 and 10.3% (Fig. 3). Notably, the k_2 values were an order of magnitude lower than the k_1 values, confirming distinct kinetic behavior (Fig. 2b).

For both NOL–Mn oxide interactions, the modeled Mn species proportions vary across individual measurements (Fig. 3). Additionally, the modeled rate constants satisfied the

condition $k_1 \geq 3k_2$, which is used to differentiate ligands based on their binding affinities and strengths.[14]

3.3.3 Manganese speciation analysis. In this study, the speciation analysis of Mn_T was performed including Mn^{2+}, $Mn^{3+}-NOL_{weak}$ complexes, and $Mn^{3+}-NOL_{strong}$ complexes. Fig. 4 shows the percentage of Mn_T that are $Mn^{3+}-NOL$ complexes (sum of $Mn^{3+}-NOL_{weak}$ and $Mn^{3+}-NOL_{strong}$ complexes) for the NOL–birnessite and the NOL–manganite interaction as a function of pH (3–7) and time (1–168 h). The formation and stabilization of $Mn^{3+}-NOL$ complexes was dependent on the individual Mn oxide, showing sharp decreases with lowering pH and increasing reaction time (strongly acidic conditions) (Fig. 4). Notably, our analysis of molar Mn_T : DOC ratios indicates that values ≥0.08 resulted in a sharp decrease in $Mn^{3+}-NOL$ complex proportions (Tables S4 and S5). The molar ratios exceeded this threshold multiple times, especially under strongly acidic conditions and reaction times ≥6 h.

For the birnessite batch experiments, the $Mn^{3+}-NOL$ complex proportions ranged from 0 to 87 ± 18% across all pH and time steps (Fig. 4a). The highest proportion of $Mn^{3+}-NOL$ complexes was observed at pH 7 after 24 h. Under circumneutral conditions, $Mn^{3+}-NOL$ complexes predominated at all time steps ranging from 68 ± 9 to 87 ± 18%. A strong contrast with low $Mn^{3+}-NOL$ complex proportions (6 ± 4 to 11 ± 7%) was observed at pH 5 between 1 and 6 h. The sharp decrease in $Mn^{3+}-NOL$ complexes within the NOL–birnessite interactions resulted from the modeling process. The parameterization of the rate constants narrowly missed the condition $k_1 \geq 3k_2$ (Table S2). The $Mn^{3+}-NOL_{weak}$ complexes could not, therefore, be modeled. Subsequently, the proportions (35 ± 4 to 86 ± 5%) increased sharply from 12 h onwards. An opposite pattern was

identified under strongly acidic conditions. $Mn^{3+}-NOL$ complexes dominated at pH 4 from 1 to 6 h; and at pH 3 only at 1 h but with a high proportion of 85 ± 9%. Remarkably, $Mn^{3+}-NOL$ complexes decreased with decreasing pH and increasing time, becoming negligible after 6 h (pH 3 and 4). Interestingly, the proportions of $Mn^{3+}-NOL$ complexes were mainly assigned to the $Mn^{3+}-NOL_{weak}$ complexes, as shown in Table S3, which is in contrast to the NOL–manganite interaction.

In summary, birnessite batch experiments indicate that $Mn^{3+}-NOL$ complexes can be predominant under all pH conditions, but the formation and stability is strongly dependent on the reaction time under strongly acidic conditions.

Fig. 4b shows the proportions of Mn_T that are $Mn^{3+}-NOL$ complexes observed in the manganite batch experiments. Overall, the $Mn^{3+}-NOL$ complex proportions ranged from 0 to 69 ± 14%. Looking closely at the pH steps, a different pattern of the $Mn^{3+}-NOL$ complex distribution becomes apparent. The highest $Mn^{3+}-NOL$ complex proportions were detected at circumneutral pH. A pH ≤ 6 already leads to a sharp decrease in the $Mn^{3+}-NOL$ complex proportions. Similar to birnessite, the proportions decreased with time. In particular, the maximum proportion of $Mn^{3+}-NOL$ complexes (69 ± 14%) was recorded at pH 7 after 12 h. Furthermore, a consistent but decreasing dominance of $Mn^{3+}-NOL$ complexes was observed only at pH 7 from 12 to 48 h (69 ± 14 to 65 ± 7%). Under both moderately and strongly acidic conditions, the $Mn^{3+}-NOL$ complex proportions decreased drastically, ranging between 0 and 21 ± 7% (pH 6, 1 h). Exceptions were observed at pH 4 after 3 h (39 ± 6%) and at pH 3 after 1 h (57 ± 4%). All modeled proportions of $Mn^{3+}-NOL$ complexes were predominantly attributed to $Mn^{3+}-NOL_{strong}$ complexes (Table S3).
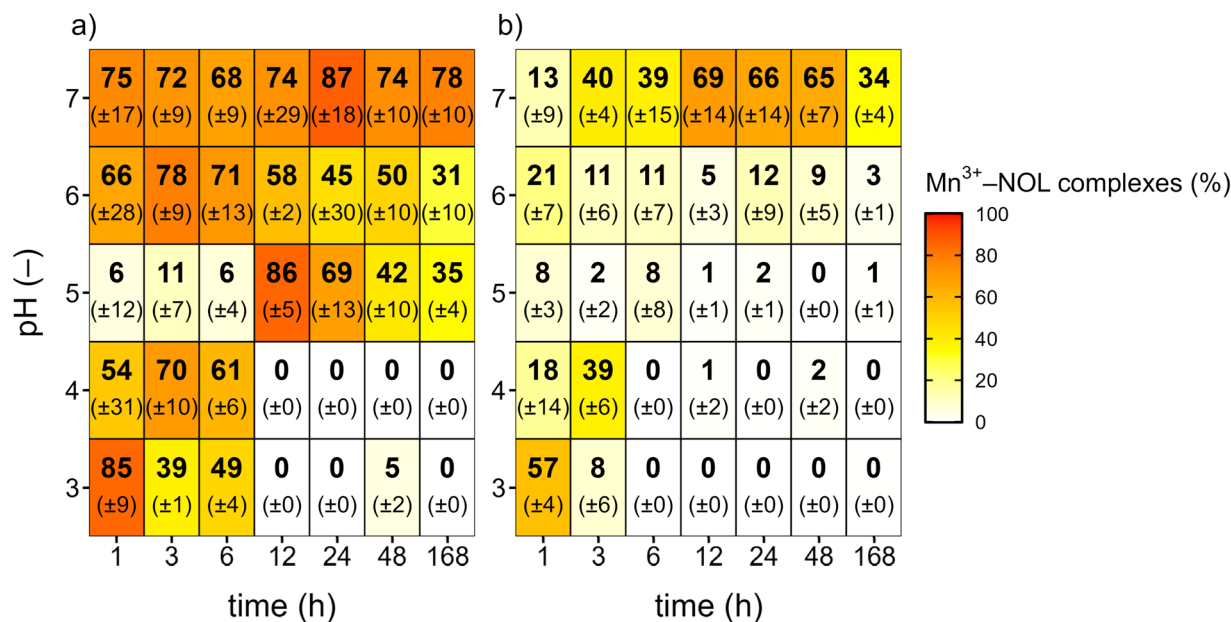

Fig. 4 Proportions of $Mn^{3+}-NOL$ complexes (%) (sum of $Mn^{3+}-NOL_{weak}$ and $Mn^{3+}-NOL_{strong}$ complexes) for (a) the NOL–birnessite and (b) the NOL–manganite interaction as a function of pH (−) and time (h) relative to Mn_T. NOL = natural organic ligand; $Mn^{3+}-NOL_{weak}$ = weakly bound Mn^{3+}; $Mn^{3+}-NOL_{strong}$ = strongly bound Mn^{3+}.

2882 | *Environ. Sci.: Processes Impacts*, 2025, **27**, 2875–2893

This journal is © The Royal Society of Chemistry 2025

To sum up, the results of the manganite batch experiments show that pH is undoubtedly the critical parameter, while the influence of time is only assumed for strongly acidic conditions and a reaction time >3 h.

For all samples in both series of batch experiments, the condition $k_1 \geq 3*k_2$ was fulfilled in the modeling process.[14] This provides evidence for the presence of Mn^{3+}–NOL_{weak} complexes, in addition to dissolved Mn^{2+} (Tables S2 and S3).

3.3.4 Concentrations and properties of the natural organic ligands. Here, we briefly outline trends that affect the formation of Mn^{3+}–NOL complexes. All DOM-batch solutions were within ±0.2 of the target pH after the batch experiments. Accordingly, the initial acid/base additions compensated for a possible pH increase induced by sorption processes (*e.g.*, ligand exchange), dissolution processes (*e.g.*, NOL-induced or H^+-promoted) and redox reactions.

For both Mn oxides, we observed that (i) strongly acidic conditions (pH 3 and 4) particularly promoted a loss in DOC (DOC_{loss}) (Table S4 and S5), while (ii) reaction time exclusively mattered in the birnessite batch experiments for pH 3–6 at 168 h (Table S4).

During the birnessite batch experiments, mean values of DOC_{loss} ranged from 2.3 ± 1.8 to 38.4 ± 2.1% with an overall mean of 15.5 ± 11.2%. At pH 7, consistently low mean DOC_{loss} proportions (7.3 ± 4.0%) were recorded, ranging from 4.3 ± 1.4 to 9.8 ± 2.1%. In contrast, sharp increases were observed at pH 3 (29.4 ± 4.5%) between 24.0 ± 3.0 and 32.9 ± 3.9%. Strikingly, mean DOC_{loss} proportions (≥29.8 ± 1.7%) at pH 4–6 increased significantly at 168 h (Table S4). Overall, a DOC_{loss} was identified with increasing time relative to the initial DOC concentrations of the DOM-batch solution for each of the five pH steps (Table S4).

DOC_{loss} proportions observed in manganite batch experiments showed a narrower range from 3.2 ± 0.6 to 22.9 ± 4.1% (Table S5) over all pH steps but a similar overall mean of 13.1 ± 7.0%. Consistently low mean DOC_{loss} proportions were recorded at pH 7 (5.6 ± 4.0%), ranging from 3.2 ± 0.6 to 10.3 ± 4.7%. Similar to birnessite, the loss of DOC was promoted under strongly acidic conditions. The highest average amounts were found at pH 4 (18.5 ± 5.4%) between 11.7 ± 0.5 and 21.6 ± 5.3%, and mean proportions at pH 3 (18.3 ± 5.4%) were nearly identical, ranging from 11.9 ± 6.3 to 22.9 ± 4.1%. However, a DOC loss promoted by increasing reaction time was not observed. Remarkably, the highest mean DOC_{loss} amounts recorded during manganite batch experiments were almost half as high (59.6%) as during the birnessite batch experiments.

UV/Vis spectroscopy analysis revealed a pH dependence for the S_S and S_RS data in the birnessite batch experiments (Table S4). Under strongly acidic conditions, the parameters showed increased values compared to moderately and circumneutral conditions, peaking at 168 h.

Similar trends were detected in the manganite batch experiments (Table S5). Though, the differences are not so pronounced and only the S_S showed clear maxima after 168 h. Additionally, MA_{254} and MA_{350} values were relatively decreased

under strongly acidic conditions compared to moderately acidic conditions and circumneutral conditions.

4 Discussion

4.1 Possible dissolution mechanisms

Fig. 5 and 6 summarize the possible abiotic pathways enabling the Mn^{3+}–NOL complex formation during our batch experiments, while biological reduction was excluded.
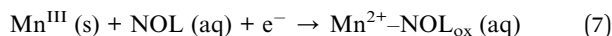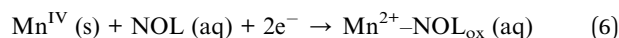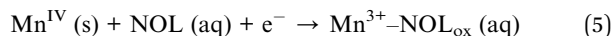
Biotic processes are mostly inactivated by NaN_3 but the activity of Gram-positive bacteria such as actinomycetes is only partially suppressed or even not affected.[78] Therefore, microbially-mediated processes like DOC degradation, resynthesis, and transformation cannot be completely excluded. Nevertheless, microbial activity should be largely restricted in this study and we focus solely on abiotic processes. These abiotic NOL–Mn oxide interactions can be categorized into four possible dissolution mechanisms (Fig. 5 and 6):

(1) Ligand-promoted non-reductive dissolution, (2) ligand-promoted reductive dissolution, (3) H^+-promoted dissolution, and (4) ligand exchange.

Looking at the NOL–birnessite interactions (Fig. 5), ligand-promoted non-reductive dissolution is a possible mechanism under circumneutral and moderately acidic conditions. Surface-bound Mn^{III} is dissolved by the adsorption of a near-associated NOL and released as a Mn^{3+}–NOL complex,[12] while the NOL is neither oxidized nor reduced [eqn (4)]. Because the AOS of the birnessite used in this study clearly indicates an increased proportion of Mn^{III}, we expect the mechanism to support the Mn^{3+}–NOL complex formation (Table S1).

$$Mn^{III} \text{ (s)} + NOL \text{ (aq)} \rightarrow Mn^{3+}\text{–NOL (aq)} \qquad (4)$$

The second mechanism involves ligand-promoted reductive dissolution (1-e^- or 2-e^- transfer) of mineral-bound Mn^{III} and Mn^{IV} by a directly associated NOL. Consequently, Mn oxide reduction and NOL oxidation proceed in parallel [eqn (5), (6) and (7)] and the same NOL forms either a Mn^{3+}–NOL complex or a Mn^{2+}–NOL complex. Alternatively, the NOL detaches Mn^{2+} or Mn^{3+} as it is oxidized, and another NOL from the solution may form a Mn^{3+}–NOL complex or a Mn^{2+}–NOL complex [eqn (5), (6) and (7)]. Banerjee and Nesbitt (1999, 2001)[22,79] stated that the reduction of birnessite is controlled by a 1-e^- transfer reaction from Mn^{IV} to Mn^{III}, forming a strong Mn^{3+} carboxyl surface complex.

$$Mn^{IV} \text{ (s)} + NOL \text{ (aq)} + e^- \rightarrow Mn^{3+}\text{–}NOL_{ox} \text{ (aq)} \qquad (5)$$

$$Mn^{IV} \text{ (s)} + NOL \text{ (aq)} + 2e^- \rightarrow Mn^{2+}\text{–}NOL_{ox} \text{ (aq)} \qquad (6)$$

$$Mn^{III} \text{ (s)} + NOL \text{ (aq)} + e^- \rightarrow Mn^{2+}\text{–}NOL_{ox} \text{ (aq)} \qquad (7)$$

EEM spectroscopy revealed humic proportions containing hydroquinones and thus phenolic groups. We assume that these functional groups contribute to homolytic 1-e^- transfers mediated by the formation of radical semiquinones in the hydroquinone/quinone system, or by intermediate phenoxy radicals. Ligand-promoted reductive dissolution is surface-

This journal is © The Royal Society of Chemistry 2025

Environ. Sci.: Processes Impacts, 2025, **27**, 2875–2893 | **2883**
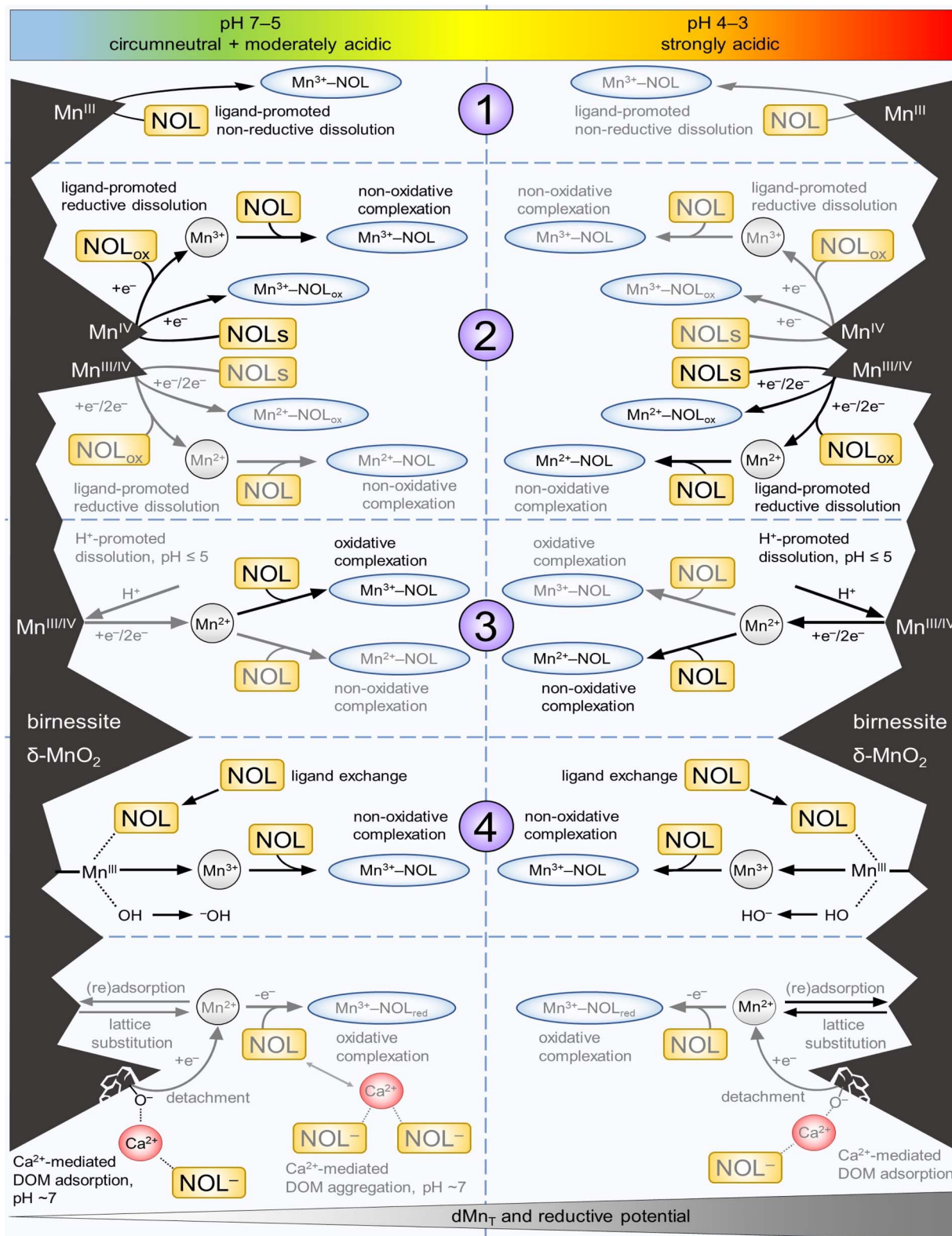
Fig. 5 Schematic illustration of the assumed essential (black) and side (gray) NOL–birnessite interactions and the proposed parallel main (black) and minor (grey) ad-/desorption processes that lead to the formation of Mn^{3+}–NOL complexes. NOL = natural organic ligand; Mn^{3+}–NOL_{weak} = weakly bound Mn^{3+}; Mn^{3+}–NOL_{strong} = strongly bound Mn^{3+}.
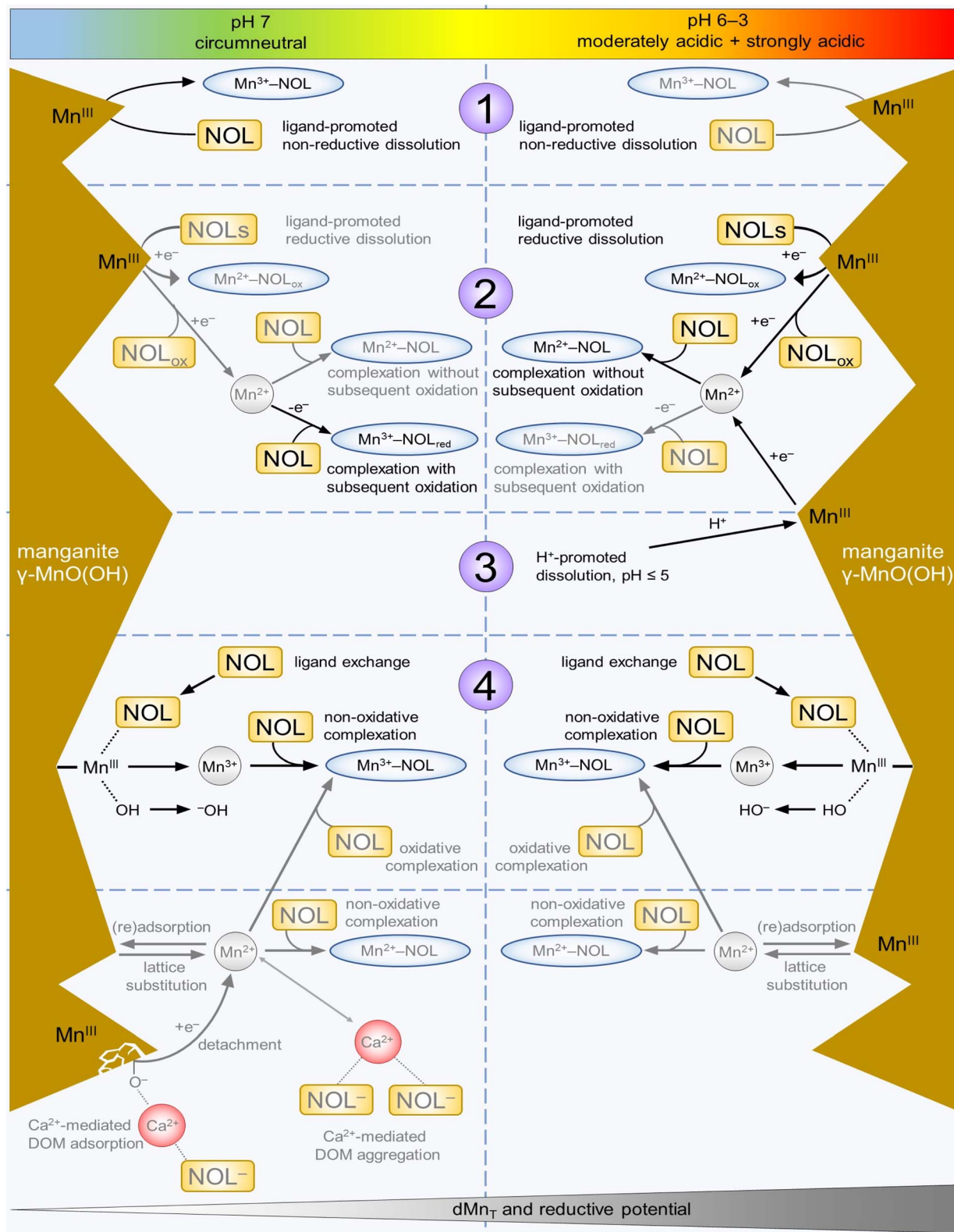
Fig. 6   Schematic illustration of the assumed essential (black) and side (gray) NOL–manganite interactions and the proposed parallel main (black) and minor (grey) ad-/desorption processes that lead to the formation of Mn^{3+}–NOL complexes. NOL = natural organic ligand; Mn^{3+}–NOL_{weak} = weakly bound Mn^{3+}; Mn^{3+}–NOL_{strong} = strongly bound Mn^{3+}.

This journal is © The Royal Society of Chemistry 2025

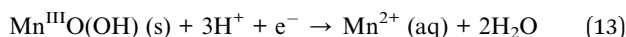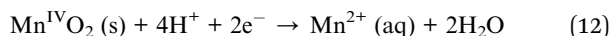Environ. Sci.: Processes Impacts, 2025, 27, 2875–2893 | 2885

controlled, requiring close association of NOLs with surface sites prior to e⁻ transfer and metal ion release.[80] Released Mn^{2+} and Mn^{3+} may subsequently be complexed by additional NOLs [eqn (8)–(10)]. Terrestrial NOLs are known to inhibit the complete oxidation of Mn^{2+} to Mn^{IV} oxides,[11,26] by stabilizing the Mn^{3+} intermediate through ligand-promoted oxidation, complexation, and simultaneous NOL reduction [eqn (9)]. Following reductive dissolution, Mn^{3+}–NOL complex formation can occur via ligand-promoted oxidative complexation similar to eqn (9). Released Mn^{2+} is complexed by NOL. The intermediate Mn^{2+}–NOL complex is then oxidized during a dark reaction promoted by reactive oxygen species, namely superoxide (O^{2-}) [eqn (11)].[11–13,81] This H^+-consuming reaction is favored under moderately to strongly acidic conditions, where high Mn oxide dissolution rates, excessive H^+ concentrations and dissolved O_2 are present.
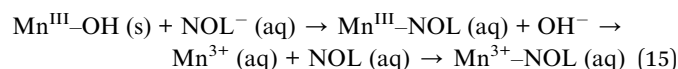
$$Mn^{3+} (aq) + NOL (aq) \rightarrow Mn^{3+}–NOL (aq) \quad (8)$$

$$Mn^{2+} (aq) + NOL (aq) \rightarrow Mn^{3+}–NOL_{red} (aq) \quad (9)$$

$$Mn^{2+} (aq) + NOL (aq) \rightarrow Mn^{2+}–NOL (aq) \quad (10)$$

$$Mn^{2+} (aq) + O_2^- + 2H^+ + NOL (aq) \rightarrow Mn^{3+}–NOL (aq) + H_2O_2 (aq) \quad (11)$$
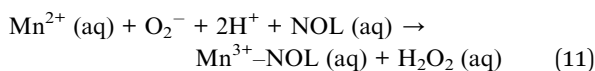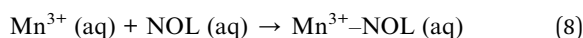
Under increasing acidic conditions, we propose H^+-promoted dissolution as the third mechanism. The observed increase in H^+-promoted background dissolution (Table S2) combined with the increasing NOL-induced dissolution (Fig. 1a) results in a decrease in Mn^{3+}–NOL complex formation. Consequently, Mn^{2+} concentrations increase, suggesting that H^+-promoted dissolution of Mn^{IV} and Mn^{III} to Mn^{2+} proceeds via a 2-e⁻ or a 1-e⁻ transfer mediated by inorganic or organic reductants [eqn (12) and (13)]. McKendry et al. (2015)[82] outlined that Mn^{III}-enriched active sites promote water oxidation and subsequent H^+ generation, which intensifies H^+-promoted background dissolution [eqn (12) and (13)]. The low AOS of our triclinic birnessite renders enhanced H^+-promoted dissolution plausible, as supported by increased initial dissolution rates and a corresponding decrease in pH.

$$Mn^{IV}O_2 (s) + 4H^+ + 2e^- \rightarrow Mn^{2+} (aq) + 2H_2O \quad (12)$$

$$Mn^{III}O(OH) (s) + 3H^+ + e^- \rightarrow Mn^{2+} (aq) + 2H_2O \quad (13)$$

In addition to the mechanisms presented in [eqn (6), (7), (12) and (13)], the sharp decrease in Mn^{3+}–NOL complex proportions (Fig. 4a) with decreasing pH and longer batch operation (>6 h) necessitates the consideration of additional mechanisms. The decay of Mn^{3+}–NOL complexes might result from internal redox reactions of organic molecules, as observed for Mn^{3+}–catechol or Mn^{3+}–citrate, leading to Mn^{2+} formation.[10,25] It is conceivable that a reduction of Mn^{3+}–NOL complexes, coupled with oxidation of ambient NOLs (1-e⁻ transfer) [eqn (14)], similar to the transformation of organic pollutants,[45,46] contributes to the decrease in Mn^{3+}–NOL complex proportions relative to Mn_T with increasing reaction time.

$$Mn^{3+}–NOL (aq) + NOL (aq) + e^- \rightarrow Mn^{2+}–NOL (aq) + NOL_{ox} (aq) \quad (14)$$
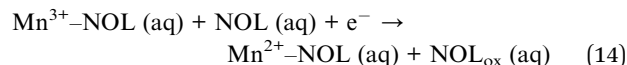
Ligand exchange, the forth possible mechanism, involves the substitution of surface hydroxyl groups (–OH) by carboxyl or phenolic groups of DOM.[3] Initial acid/base additions stabilized the pH and compensated for –OH release. NOLs adsorb to Mn centers, replacing –OH groups, weakening Mn–OH bonds,[3,83] and altering surface coordination, promoting the release of Mn^{3+}, which is subsequently complexed by additional NOLs [eqn (15)]. This mechanism is favored by NOLs with high molecular weight (HMW), acidity, and aromaticity,[3] and likely contributes to Mn^{3+}–NOL complex formation under circumneutral conditions. As noted by Stuckey et al. (2018),[83] ligand exchange may be particularly relevant under moderately to strongly acidic conditions, supporting Mn^{3+}–NOL complex formation in the early stages of the NOL–Mn oxide interactions.

$$Mn^{III}–OH (s) + NOL^- (aq) \rightarrow Mn^{III}–NOL (aq) + OH^- \rightarrow Mn^{3+} (aq) + NOL (aq) \rightarrow Mn^{3+}–NOL (aq) \quad (15)$$

Complementary to the mechanisms discussed above, Mn^{3+}–NOL complexes may be formed or degraded by additional reactions. Disproportionation of Mn^{3+}–NOL complexes [eqn (16)], as proposed for neutral pH and citrate as the chelator, may explain the small Mn^{2+} proportions at circumneutral pH (Fig. 4a).[24]

$$2Mn^{3+}–NOL (aq) + 2H_2O \rightarrow Mn^{2+}–NOL_{ox} (aq) + Mn^{IV}O_2 (s) + NOL_{ox} (aq) + 4H^+ \quad (16)$$
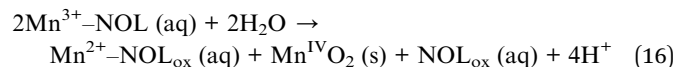
Surface-catalyzed oxidation of Mn^{2+} to Mn^{3+}, followed by complexation through additional ligands, promotes Mn^{3+}–NOL complex formation [eqn (17)].[11] In combination with eqn (11) and (15), Mn^{3+}–NOL complex concentrations increase, consistent with the rise observed at pH 5 after 12 h (Fig. 4a).

$$Mn^{2+} (aq) + surface (s) + NOL (aq) \rightarrow Mn^{3+}–NOL_{red} (aq) \quad (17)$$
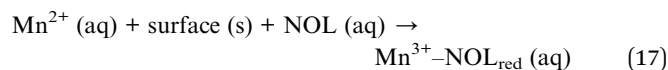
We conclude that (i) ligand-promoted non-reductive dissolution, (ii) ligand-promoted reductive dissolution either directly or followed by subsequent complexation with and without oxidation, (iii) ligand exchange, and apart from these mechanisms (iv) the observed molar $Mn_T : DOC$ ratio ≤0.08 (Table S4) promote the formation of Mn^{3+}–NOL complexes under circumneutral and moderately acidic conditions. The relatively small Mn^{2+} proportions resulted from reductive degradation of Mn^{3+}–NOL complexes, for example through redox-active transformation of additional NOLs. Contrastingly, under strongly acidic conditions (pH 3–4, >6 h), decreased Mn^{3+}–NOL complex concentrations (Fig. 4a) result from (i) lesser ligand-promoted non-reductive dissolution, (ii) dominant ligand-promoted or H^+-promoted dissolution, followed by complexation without oxidation, (iii) progressive reduction of Mn^{3+}–NOL complexes by additional NOLs, and besides these mechanisms (iv) the observed molar $Mn_T : DOC$ ratio ≥0.08 (Table S4). Since the experimental setup provides only a temporary, limited insight

2886 | Environ. Sci.: Processes Impacts, 2025, **27**, 2875–2893

This journal is © The Royal Society of Chemistry 2025

into the ongoing solution chemistry, considerable variations in the Mn^{3+}–NOL complex concentrations are expected. Overall, Mn^{3+}–NOL complexes appear to be metastable under strongly acidic conditions.

Focusing on NOL–manganite interactions (Fig. 6), (i) ligand-promoted non-reductive dissolution [eqn (4)], (ii) ligand-promoted reductive dissolution by direct complexation (1-e^- transfer) or detachment of Mn^{2+} [eqn (7)] with subsequent oxidation [eqn (9) and (11)], and (iii) ligand exchange [eqn (15)] are assumed to promote the formation of Mn^{3+}–NOL complexes under circumneutral conditions (Fig. 4b). Similar to birnessite, the observed pH drift caused by –OH release could be initialized by ligand exchange [eqn (12)].[84]

At pH ≤ 6, the strong decrease in Mn^{3+}–NOL complexes indicates a change in the predominating mechanisms. As pH decreases, the synergy between H^+-promoted and ligand-promoted reductive dissolution of surface-coordinated Mn^{III} increases.[36] Similar to birnessite, solid Mn^{III} is reductively dissolved and the corresponding NOLs are simultaneously oxidized [eqn (7)]. Additional NOLs then complex Mn^{2+} without oxidation [eqn (10)]. Manganite provides a higher E_H (1.51 V) than Mn^{IV} oxides (1.23 V) and thus, an increased potential to oxidize DOM and to be reduced.[85] Various studies have shown that manganite is reductively dissolved by a myriad of organic compounds.[26–29] The negligible traces of Mn^{3+}–NOL$_{weak}$ complexes and the small proportions of Mn^{3+}–NOL$_{strong}$ complexes are consistent with the findings by McArdell et al. (1998),[35] who studied the dissolution of $Mn^{III}O(OH)$ interacting with ligands such as aminocarboxylates.

Another reductive dissolution mechanism that increases the Mn^{2+} concentration is the H^+-promoted disproportion (pH < 6) of Mn^{III} [eqn (18)].[29,31] The precipitated MnO_2 is susceptible to reductive dissolution, potentially further increasing Mn^{2+} concentration.

$$2Mn^{III}O(OH)\ (s) + 2H^+ \rightarrow$$
$$Mn^{2+}\ (aq) + Mn^{IV}O_2\ (s) + 2H_2O \qquad (18)$$
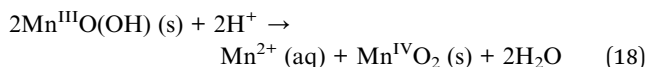
Under strongly acidic conditions, the higher proportions of Mn^{3+}–NOL complexes observed during the first 3 h can be attributed to synergistic effects of the four possible dissolution mechanisms. The variability in Mn^{3+}–NOL complex proportions highlights the unstable nature of these complexes, which are susceptible to disproportion at low pH. Additionally, they are prone to degradation via intramolecular or intermolecular e^- transfer reactions.[10,30,45,46]

In contrast to birnessite, NOL–manganite interactions favor the formation of Mn^{3+}–NOL$_{strong}$ complexes (Table S3). Whether the high Mn^{3+}–NOL$_{strong}$ complex proportions result from the individual E_H of the manganite, its predominant valence state, low SSA, surface charge, or selective NOL adsorption remains uncertain and warrants further investigation.

The formation and stabilization of Mn^{3+}–NOL complexes primarily depends on pH (key parameter), as well as on reaction time and the properties of both Mn oxides and NOLs. We assume that the predominant Mn valence of the Mn oxide governs the preferential dissolution mechanisms as a function of solution pH. However, further studies are required to qualify and quantify the influence of the dominant Mn valence.

Similar to the findings on Mn^{3+}–NOM complexes,[3] it can be confirmed from our data that lower molar Mn_T : DOC ratios (≤0.08) support the formation of Mn^{3+}–NOL complexes (Tables S4 and S5). We therefore hypothesize that NOL availability is a decisive factor. The range of Mn^{3+}–NOL complex proportions (Fig. 4) determined in this study (0 to 87 ± 18%), particularly under strongly acidic conditions during the first 6 h (0 to 85 ± 9%), aligns with our previous analyses of in situ sampled non-limed (11 to 79%) and formerly limed (10 to 87%) forest floor solutions and soil solutions.[9]

Although Mn^{2+} was the predominant species under strongly acidic conditions, Mn^{3+}–NOL complexes remain a non-negligible compound in NOL-enriched topsoil layers at the acidic forest site. However, the formation and stabilization of Mn^{3+}–NOL complexes are evidently restricted, characterizing them metastable under natural acidic conditions.

4.1.1 Possible side mechanisms. Parallel side mechanisms occur during NOL–Mn oxide interactions (Fig. 5 and 6) and affect the Mn speciation analysis.

Adsorption of released Mn^{2+} was neither qualitatively nor quantitatively assessed in this study, but it should be considered. Mn^{2+} adsorption is particularly favored by negatively charged mineral surfaces and high SSA. This surface-catalyzed process can occur under strongly to moderately acidic conditions, particularly for the synthesized birnessite, as well as under circumneutral conditions (Fig. 5). Upon adsorption onto the mineral surface, Mn^{2+} may participate in redox interactions, leading to the formation of various Mn^{3+}-containing mineral phases through comproportionation.[86,87] Alternatively, Mn^{2+} may undergo oxidation followed by precipitation, however, this process is strongly pH-dependent and thermodynamically unfavorable below pH 8.[88]

Any addition of salts to the DOM-stock solution increases the ionic strength, influences the solubility of (trace) metals, affects the binding affinity of DOM to the surfaces of the Mn oxides, and thus the dissolution kinetics and Mn speciation analysis.[89,90]

During our batch operations, the mean molarities for Ca^{2+} ranged from 0.0003 to 0.001 M (Tables S6 and S7). This cation mediates interactions between negatively charged NOLs, in particular carboxyl groups, and negatively charged Mn oxide surfaces by the formation of inner- and outer-sphere surface complexes and/or electrostatic attraction.[90] Experimental indications of this side mechanism were found during the NOL–Mn oxide interactions at pH 7 for birnessite at all time steps and more limited for manganite at ≥12 h (Fig. 5 and 6). By this mechanism, the NOLs are (temporarily) removed from the solution and are not available for, amongst others, the complexation of dissolved Mn^{2+} with or without oxidation [eqn (8)–(10)]. This effect was indicated by a distinct decrease in the Ca^{2+} concentrations (Tables S6 and S7). However, the experimental data do not provide conclusive evidence for this mechanism and further studies are needed. By contrast, this mechanism did not occur reliably under strongly acidic conditions, since Ca^{2+} then has a lower sorption affinity towards Mn

This journal is © The Royal Society of Chemistry 2025

Environ. Sci.: Processes Impacts, 2025, 27, 2875–2893 | **2887**

oxides[91,92] and is displaced by (excessively) released Mn^{2+} and H^+.[93] Looking at manganite, its high PZC and smaller SSA limit the readsorption rate.

Another possible side mechanism involves the formation of Ca^{2+}-mediated DOM aggregates, leading to HMW organic molecules.[94] It occurs preferentially under circumneutral conditions, as carboxyl groups are mainly deprotonated. Although HMW NOLs are more prevalent under circumneutral conditions, this process cannot be conclusively verified by the data. Similar effects do not occur in Na^+ and Mg^{2+} solutions.[95] For mechanisms such as cation bridging and aggregate formation, the influence of NaN_3 and $NaOH$ which were used in our experiments is negligible. However, NaN_3 can act as both an oxidant and a reductant, potentially altering DOM molecules (e.g., quinones and phenols) by rapidly reducing redox-active functional groups, thereby decreasing their overall reducing capacity.[96] Since a control experiment without NaN_3 was not performed, a potential influence of NaN_3 on the reducing capacity of DOM or the EEM spectroscopy analysis cannot be excluded.

4.1.2 Interactions of the natural organic ligands. During the batch experiments, the observed DOC_{loss} proportions may result from (i) adsorption onto mineral surfaces, (ii) surface-catalyzed degradation to CO_2,[97] and (iii) the formation and precipitation of non-filter-passing $Mn^{2+/3+}$ colloids stabilized by humic acids.[3,97] These processes alter the DOM composition, thereby influencing Mn^{3+}–NOL complex formation and, consequently, Mn speciation analysis.

For birnessite, increased DOC_{loss} proportions (pH $\leq$ 4) are attributed to its high SSA and surface charge, which promote adsorption, higher sorption capacities (e.g., Mn^{2+}, DOM),[83,98] dissolution kinetics,[31] and oxidation of many polar organic compounds.[85] Protonated functional groups like carboxyl (pK_a 3–6)[99] and phenolic groups (pK_a 8–11)[100] are less repelled by the negatively charged surface. Adsorption is largely governed by carboxyl groups, which are abundant alongside hydroxylic groups in terrestrial DOM.[101] These groups initiate bridging and/ or the mono-/bidentate bonds that bind DOM to birnessite.[102] Once adsorbed, DOM is prone to surface-catalyzed oxidation, as indicated by increased Ss and S_R values (Table S4). Birnessite is known for its ability to oxidize organic molecules such as catechol to CO_2, releasing Mn^{2+}. This process contributes to a progressive DOC loss over time, which further shifts the Mn_T: DOC ratio, preventing the formation of Mn^{3+}–NOL complexes.

For manganite, the almost halved DOC_{loss} (pH $\leq$ 4) compared to birnessite results from its small SSA and repelled functional groups due to the mineral surface charge. Decreased MA_{254} and MA_{350} values, along with increased Ss and S_RS, suggest shrinking aromaticity and a predominance of LMW NOLs (Table S5). This aligns with the preferential adsorption of molecules with HMW, high(er) aromaticity, high content of oxygen, nitrogen and carbohydrates, while unsaturated LMW molecules, defined by less oxygen-containing functional groups, remain dissolved.[3,97,103] Ongoing oxidation of DOM, driven by the strong oxidative potential of manganite as well as the higher reductive potential of the solution, leads to its degradation. Consequently, terrestrial LMW NOLs complex Mn^{3+} only to a limited extent and the resulting Mn^{3+}–NOL

complexes are metastable, particularly under strongly acidic conditions.

Considering the general binding affinity of NOLs under strongly acidic conditions, Mn^{2+} and H^+ are assumed to compete for binding sites on NOLs, such as humic acids.[104] This competitive binding, resulted by reductive dissolution mechanisms and a molar Mn_T: DOC ratio ≥ 0.08, strongly hinders Mn^{3+}–NOL complex formation.

In summary, concentration, availability, composition (e.g., functional groups, charge) and potential transformation of DOM during NOL–Mn oxide interactions are crucial for Mn^{3+}–NOL complex formation.

4.2 Method criticism

The extraction protocol for the forest floor solution affects the duration of extraction, the dissolution ratio,[105] the concentration of the background electrolyte,[77,106] and the intensity of rewetting of the dried forest soil sample.[107] Consequently, the protocol for the extraction of NOLs has a decisive influence on the NOL concentration, composition, and reactivity.[108] In addition, micro- and nano-sized Mn oxides that surpass the filtration steps cannot be completely excluded and might lead to an overestimation of Mn^{3+}–NOL_{strong} complexes.[30]

Looking at the kinetic modeling process, unknown environmental samples with their individual reaction kinetics are challenging. In particular, a large number of unknown NOLs complicate the modeling and parameterization.[9,109] The equations used for modeling [eqn (1) and (2)] are simplified and represent the diversity of the NOL pool only to a limited extent. More precise kinetic modeling would require extending these equations to account for the individual number of NOLs, as suggested by Kim et al. (2022).[109] Furthermore, due to the largy variety of NOLs, it remains unclear whether certain NOLs withstand competition from T(4-CP)P[30] or hydroxylamine. Consequently, it is impossible to fully incorporate the variability of unknown NOLs into the modeling process.

Additionally, the use of experimental and analytical triplicates introduces further variability into the Mn_T pool data. This variability arises from (i) the individual DOM composition of each replicate (ii) minor inconsistencies in manual procedures (e.g., pipetting), and (iii) the process of fitting experimental data to the model equations.

We are critically aware that, in particular, the removal of Al^{3+} and Fe^{3+} species by the cation exchange resin excluded prominent binding partners for NOLs. Under natural conditions, these cations form stable complexes with the NOLs of the soil solution[110] and thus compete with dissolved Mn species. It is, therefore, obvious that natural soil solutions exhibit a more variable cation pool. We conclude that additional competitive side reactions potentially decrease Mn^{3+}–NOL complex concentrations, resulting in increased Mn^{2+} proportions.

5. Conclusions

Our results demonstrate that Mn^{3+}–NOL complexes are important constituents of the Mn_T pool in forest floor solutions. We

2888 | Environ. Sci.: Processes Impacts, 2025, **27**, 2875–2893

This journal is © The Royal Society of Chemistry 2025

further outline fundamental abiotic mechanisms that are assumed to contribute to the formation of Mn^{3+}–NOL complexes in terrestrial environments. Since its formation and stability are particularly limited under strongly acidic conditions, it is a metastable species that is subject to a continuous cycle of formation and decay. However, Mn^{3+}–NOL complexes remain a non-negligible compound. It is likely that high amounts of reactive Mn^{3+}–NOL complexes promote the oxidative degradation of organic compounds as well as altering the acidity and redox capacity of forest floor solutions. Consequently, the role of Mn^{3+}–NOL complexes in terrestrial environments has been underestimated. Based on our findings, we hypothesize that different types of Mn oxides react with NOLs to enable the formation of Mn^{3+}–NOL complexes over a wide pH range in forest floor solutions, even under oxidizing conditions. Further research should investigate more complex forest floor and soil solution matrices as well as different Mn oxides, and follow the trace of Mn^{3+}–NOL complexes.

Conflicts of interest

The authors declare that there are no conflicts of interest.

Data availability

The data supporting this article have been included as part of the SI. See DOI: **https://doi.org/10.1039/d5em00388a**.

Acknowledgements

References

1 Z. L. He, J. Shentu and X. E. Yang, in *Trace Elements in Soils*, ed. P. S. Hooda, Wiley, West Sussex, 1st edn, 2010, ch. 20, pp. 481–495.

2 N. Wiberg, E. Wiberg and A. F. Hollemann, in *Anorganische Chemie, Band 2*, ed. N. Wiberg, de Gruyter, Berlin, 103rd edn, 2017, ch. XXVIII, pp. 1899–1933.

3 H. Li, F. Santos, K. Butler and E. Herndon, A Critical Review on the Multiple Roles of Manganese in Stabilizing and Destabilizing Soil Organic Matter, *Environ. Sci. Technol.*, 2021, **55**, 12136–12152.

4 G. Biedermann and R. Palombari, On the Hydrolysis of Manganese(III) Ion, *Acta Chem. Scand. A*, 1978, **32**, 381–390.

5 G. Davies, Some Aspects of Chemistry of Manganese(III) in Aqueous Solution, *Coordin. Chem. Rev.*, 1969, **4**, 199–224.

6 K. L. Johnson, C. M. McCann, J.-L. Wilkinson, M. Jones, B. M. Tebo, M. West, C. Elgy, C. E. Clarke, C. Gowdy and K. A. Hudson-Edwards, Dissolved Mn(III) in water treatment works: Prevalence and significance, *Water Res.*, 2018, **140**, 181–190.

7 A. S. Madison, B. M. Tebo and G. W. Luther, 3rd, Simultaneous determination of soluble manganese(III), manganese(II) and total manganese in natural (pore) waters, *Talanta*, 2011, **84**, 374–381.

8 G. W. Luther, A. S. Madison, A. Mucci, B. Sundby and V. E. Oldham, A kinetic approach to assess the strengths of ligands bound to soluble Mn(III), *Mar. Chem.*, 2015, **173**, 93–99.

9 C. Lux and T. Mansfeldt, Evidence of dissolved trivalent manganese in acidic forest soils, *J. Plant Nutr. Soil Sci.*, 2023, **186**, 321–329.

10 V. E. Oldham, S. M. Owings, M. R. Jones, B. M. Tebo and G. W. Luther, Evidence for the presence of strong Mn(III)-binding ligands in the water column of the Chesapeake Bay, *Mar. Chem.*, 2015, **171**, 58–66.

11 V. E. Oldham, A. Mucci, B. M. Tebo and G. W. Luther, 3rd, Soluble Mn(III)–L complexes are abundant in oxygenated waters and stabilized by humic ligands, *Geochim. Cosmochim. Acta*, 2017, **199**, 238–246.

12 V. E. Oldham, M. T. Miller, L. T. Jensen and G. W. Luther, Revisiting Mn and Fe removal in humic rich estuaries, *Geochim. Cosmochim. Acta*, 2017, **209**, 267–283.

13 V. E. Oldham, M. R. Jones, B. M. Tebo and G. W. Luther, Oxidative and reductive processes contributing to manganese cycling at oxic-anoxic interfaces, *Mar. Chem.*, 2017, **195**, 122–128.

14 A. Thibault de Chanvalon and G. W. Luther, Mn speciation at nanomolar concentrations with a porphyrin competitive ligand and UV-vis measurements, *Talanta*, 2019, **200**, 15–21.

15 L. A. Sparrow and N. C. Uren, Manganese oxidation and reduction in soils: effects of temperature, water potential, pH and their interactions, *Soil Res.*, 2014, **52**, 483–494.

16 X. H. Feng, L. M. Zhai, W. F. Tan, F. Liu and J. Z. He, Adsorption and redox reactions of heavy metals on synthesized Mn oxide minerals, *Environ. Pollut.*, 2007, **147**, 366–373.

17 J. E. Post, Manganese oxide minerals: Crystal structures and economic and environmental significance, *Proc. Natl. Acad. Sci. U. S. A.*, 1999, **96**, 3447–3454.

18 S. T. Martin, in *Environmental Catalysis*, ed. V. H. Grassian, CRC Press, New York, 1st edn, 2005, ch. 3, pp. 61–82.

19 B. M. Tebo, J. R. Bargar, B. G. Clement, G. J. Dick, K. J. Murray, D. Parker, R. Verity and S. M. Webb, BIOGENIC MANGANESE OXIDES: Properties and Mechanisms of Formation, *Annu. Rev. Earth Planet. Sci.*, 2004, **32**, 287–328.

20 A.-C. Gaillot, V. A. Drits, A. Manceau and B. Lanson, Structure of the synthetic K-rich phyllomanganate birnessite obtained by high-temperature decomposition of

This journal is © The Royal Society of Chemistry 2025

Environ. Sci.: Processes Impacts, 2025, **27**, 2875–2893 | **2889**

KMnO$_4$: Substructures of K-rich birnessite from 1000 °C experiment, *Micropor. Mesopor. Mat.*, 2007, **98**, 267–282.

21 D. C. Golden, J. B. Dixon and C. C. Chen, Ion Exchange, Thermal Transformations, and Oxidizing Properties of Birnessite, *Clay Clay Miner.*, 1986, **34**, 511–520.

22 D. Banerjee and H. W. Nesbitt, XPS study of reductive dissolution of birnessite by oxalate: Rates and mechanistic aspects of dissolution and redox processes, *Geochim. Cosmochim. Acta*, 1999, **63**, 3025–3038.

23 G. R. Aiken, H. Hsu-Kim and J. N. Ryan, Influence of dissolved organic matter on the environmental fate of metals, nanoparticles, and colloids, *Environ. Sci. Technol.*, 2011, **45**, 3196–3201.

24 J. K. Klewicki and J. J. Morgan, Kinetic behavior of Mn(III) complexes of pyrophosphate, EDTA, and citrate, *Environ. Sci. Technol.*, 1998, **32**, 2916–2922.

25 J. K. Klewicki and J. J. Morgan, Dissolution of β-MnOOH particles by ligands: Pyrophosphate, ethylenediaminetetraacetate, and citrate, *Geochim. Cosmochim. Acta*, 1999, **63**, 3017–3024.

26 Y. Wang and A. T. Stone, Reaction of Mn^{III,IV} (hydr)oxides with oxalic acid, glyoxylic acid, phosphonoformic acid, and structurally-related organic compounds, *Geochim. Cosmochim. Acta*, 2006, **70**, 4477–4490.

27 Y. Wang and A. T. Stone, Phosphonate- and carboxylate-based chelating agents that solubilize (hydr)oxide-bound Mn^{III}, *Environ. Sci. Technol.*, 2008, **42**, 4397–4403.

28 O. W. Duckworth and G. Sposito, Siderophore–manganese(III) interactions. I. Air-oxidation of manganese(II) promoted by desferrioxamine B, *Environ. Sci. Technol.*, 2005, **39**, 6037–6044.

29 O. W. Duckworth and G. Sposito, Siderophore–manganese(III) interactions II. Manganite dissolution promoted by desferrioxamine B, *Environ. Sci. Technol.*, 2005, **39**, 6045–6051.

30 X. Wang, M. R. Jones, Z. Pan, X. Lu, Y. Deng, M. Zhu and Z. Wang, Trivalent manganese in dissolved forms: Occurrence, speciation, reactivity and environmental geochemical impact, *Water Res.*, 2024, **263**, 122198.

31 M. Ramstedt and S. Sjöberg, Phase Transformations and Proton Promoted Dissolution of Hydrous Manganite (γ-MnOOH), *Aquat. Geochem.*, 2005, **11**, 413–431.

32 D. R. Lovley and E. J. P. Phillips, Novel Mode of Microbial Energy Metabolism: Organic Carbon Oxidation Coupled to Dissimilatory Reduction of Iron or Manganese, *Appl. Environ. Microb.*, 1988, **54**, 1472–1480.

33 C. R. Myers and K. H. Nealson, Bacterial Manganese Reduction and Growth with Manganese Oxide as the Sole Electron Acceptor, *Science*, 1988, **240**, 1319–1321.

34 J. E. Johnson, P. Savalia, R. Davis, B. D. Kocar, S. M. Webb, K. H. Nealson and W. W. Fischer, Real-Time Manganese Phase Dynamics during Biological and Abiotic Manganese Oxide Reduction, *Environ. Sci. Technol.*, 2016, **50**, 4248–4258.

35 C. S. McArdell, A. T. Stone and J. Tian, Reaction of EDTA and related aminocarboxylate chelating agents with

36 A. T. Stone and J. J. Morgan, Reduction and Dissolution of Manganese(III) and Manganese(IV) Oxides by Organics. 1. Reaction with Hydroquinone, *Environ. Sci. Technol.*, 1984, **18**, 450–456.

37 A. G. Xyla, B. Sulzberger, G. W. Luther IIIrd, J. G. Hering, P. Van Cappellen and W. Stumm, Reductive Dissolution of Manganese(III,IV) (Hydr)oxides by Oxalate: The Effect of pH and Light, *Langmuir*, 1992, **8**, 95–103.

38 S. Zhang, B. Li, Y. Chen, M. Zhu, J. A. Pedersen, B. Gu, Z. Wang, H. Li, J. Liu, X.-Q. Zhou, Y.-Y. Hao, H. Jiang, F. Liu, Y.-R. Liu and H. Yin, Methylmercury Degradation by Trivalent Manganese, *Environ. Sci. Technol.*, 2023, **57**, 5988–5998.

39 B. Berg, K. T. Steffen and C. McClaugherty, Litter decomposition rate is dependent on litter Mn concentrations, *Biogeochem.*, 2007, **82**, 29–39.

40 M. Hofrichter, Review: lignin conversion by manganese peroxidase (MnP), *Enzyme Microb. Technol.*, 2002, **30**, 454–466.

41 M. E. Jones, P. S. Nico, S. Ying, T. Regier, J. Thieme and M. Keiluweit, Manganese-Driven Carbon Oxidation at Oxic–Anoxic Interfaces, *Environ. Sci. Technol.*, 2018, **52**, 12349–12357.

42 M. E. Jones, R. E. LaCroix, J. Zeigler, S. C. Ying, P. S. Nico and M. Keiluweit, Enzymes, Manganese, or Iron? Drivers of Oxidative Organic Matter Decomposition in Soils, *Environ. Sci. Technol.*, 2020, **54**, 14114–14123.

43 M. Keiluweit, P. Nico, M. E. Harmon, J. Mao, J. Pett-Ridge and M. Kleber, Long-term litter decomposition controlled by manganese redox cycling, *Proc. Natl. Acad. Sci. U. S. A.*, 2015, **112**, E5253–E5260.

44 J. Stendahl, B. Berg and B. D. Lindahl, Manganese availability is negatively associated with carbon storage in northern coniferous forest humus layers, *Sci. Rep.*, 2017, **7**, 15487.

45 E. Hu, Y. Zhang, S. Wu, J. Wu, L. Liang and F. He, Role of dissolved Mn(III) in transformation of organic contaminants: Non-oxidative *versus* oxidative mechanisms, *Water Res.*, 2017, **111**, 234–243.

46 X. Wang, J. Yao, S. Wang, X. Pan, R. Xiao, Q. Huang, Z. Wang and R. Qu, Phototransformation of estrogens mediated by Mn(III), not by reactive oxygen species, in the presence of humic acids, *Chemosphere*, 2018, **201**, 224–233.

47 *Forschungsanstalt für Waldökologie und Forstwirtschaft Rheinland-Pfalz (FAWF), Dauerbeobachtungsfläche 101: Idar-Oberstein (Umweltkontrollstation)*, https://fawf.wald.rlp.de/indexphp?id=12306, accessed May 2025.

48 IUSS Working Group WRB, *World Reference Base for Soil Resources. International Soil Classification System for Naming Soils and Creating Legends for Soil Maps*, International Union of Soil Sciences (IUSS), Vienna, Austria, 2022, 4th edn https://www.isric.org/sites/default/files/WRB_fourth_edition_2022-12-18.pdf, accessed May 2025.

Co(III)OOH (heterogenite) and Mn(III)OOH (manganite), *Environ. Sci. Technol.*, 1998, **32**, 2923–2930.

2890 | *Environ. Sci.: Processes Impacts*, 2025, **27**, 2875–2893

This journal is © The Royal Society of Chemistry 2025

49 Soil Science Division Staff, Examination and Description of Soil Profiles, in *Soil Survey Manual*, ed. C. Ditzler, K. Scheffe and H. C. Monger, USDA Handbook, 2018, **18**, ch. 3, pp. 83–233.

50 *Ad-hoc-Arbeitsgruppe Boden, Bodenkundliche Kartieranleitung (KA5), Bundesanstalt für Geowissenschaften und Rohstoffe*, Hannover, 6th edn, 2025.

51 GAFA, Handbuch Forstliche Analytik (HFA), 1. – 6, Ergänzung des Gutachterausschuss Forstliche Analytik, *Bundesministerium für Ernährung, Landwirtschaft und Verbraucherschutz (BMELV) & Nordwestdeutsche Forstliche Versuchsanstalt (NWFVA)*, **https://blumwald.thuenen.de/fileadmin/blumwald/BZE/HFA_Gesamtdatei_2022.pdf**, accessed May 2025.

52 F. Amery, F. Degryse, W. Degeling, E. Smolders and R. Merckx, The Copper-Mobilizing-Potential of Dissolved Organic Matter in Soils Varies 10-Fold Depending on Soil Incubation and Extraction Procedures, *Environ. Sci. Technol.*, 2007, **41**, 2277–2281.

53 V. J. G. Houba, I. Novozamsky, Th. M. Lexmond and J. J. van der Lee, Applicability of 0.01 M CaCl2 as a single extraction solution for the assessment of the nutrient status of soils and other diagnostic purposes, *Commun. Soil Sci. Plan.*, 1990, **21**, 2281–2290.

54 M. R. Provenzano, P. Caricasole, G. Brunetti and N. Senesi, Dissolved Organic Matter Extracted With Water and a Saline Solution From Different Soil Profiles, *Soil Sci.*, 2010, **175**, 255–262.

55 B. W. Strobel, H. C. B. Hansen, O. K. Borggaard, M. K. Andersen and K. Raulund-Rasmussen, Composition and reactivity of DOC in forest floor soil solutions in relation to tree species and soil type, *Biogeochem.*, 2001, **56**, 1–26.

56 P. G.-J. de Maagd, T. L. Sinnige, S. M. Schrap, A. Opperhuizen and D. T. H. M. Sijm, Sorption coefficients of polycyclic aromatic hydrocarbons for two lake sediments: Influence of the bactericide sodium azide, *Environ. Toxicol. Chem.*, 1998, **17**, 1899–1907.

57 T. Ohno, Fluorescence inner-filtering correction for determining the humification index of dissolved organic matter, *Environ. Sci. Technol.*, 2002, **36**, 742–746.

58 C. A. Stedmon, S. Markager and R. Bro, Tracing dissolved organic matter in aquatic environments using a new approach to fluorescence spectroscopy, *Mar. Chem.*, 2003, **82**, 239–254.

59 D. M. McKnight, E. W. Boyer, P. K. Westerhoff, P. T. Doran, T. Kulbe and D. T. Andersen, Spectrofluorometric characterization of dissolved organic matter for indication of precursor organic material and aromaticity, *Limnol. Oceanogr.*, 2001, **46**, 38–48.

60 A. Zsolnay, E. Baigar, M. Jimenez, B. Steinweg and F. Saccomandi, Differentiating with fluorescence spectroscopy the sources of dissolved organic matter in soils subjected to drying, *Chemosphere*, 1999, **38**, 45–50.

61 A. Huguet, L. Vacher, S. Relexans, S. Saubusse, J. M. Froidefond and E. Parlanti, Properties of fluorescent dissolved organic matter in the Gironde Estuary, *Org. Geochem.*, 2009, **40**, 706–719.

62 P. G. Coble, Characterization of marine and terrestrial DOM in seawater using excitation–emission matrix spectroscopy, *Mar. Chem.*, 1996, **51**, 325–346.

63 R Core Team, R, *A Language and Environment for Statistical Computing, Version 4.2.2*, Vienna, Austria, 2022.

64 Posit team, RStudio, *Integrated Development Environment for R, Version 2022.12.0, Posit Software*, PBC, Boston, MA, 2022.

65 M. Pucher, U. Wünsch, G. Weigelhofer, K. Murphy, T. Hein and D. Graeber, staRdom: Versatile Software for Analyzing Spectroscopic Data of Dissolved Organic Matter in R, *Water*, 2019, **11**, 2366.

66 M. C. Rabenhorst and K. A. Persing, A Synthesized Manganese Oxide for Easily Making Durable Manganese-Coated IRIS Tubes, *Soil Sci. Soc. Am. J.*, 2017, **81**, 233–239.

67 R. Giovanoli and U. Leuenberge, Über die Oxydation von Manganoxidhydroxid, *Helv. Chim. Acta*, 1969, **52**, 2333–2347.

68 J. A. Lee, C. E. Newnham, F. S. Stone and F. L. Tye, Thermal Decomposition of Manganese Oxyhydroxide, *J. Solid State Chem.*, 1980, **31**, 81–93.

69 J. C. Nash, *nlmrt: Functions for Nonlinear Least Squares Solutions*, **https://cran.r-project.org/web/packages/nlmrt/index.html**, accessed May 2025.

70 J. C. Nash, *Compact Numerical Methods for Computers: Linear Algebra and Function Minimisation*, Adam Hilger Ltd, Bristol, 2nd edn, 1990.

71 J. L. Weishaar, G. R. Aiken, B. A. Bergamaschi, M. S. Fram, R. Fujii and K. Mopper, Evaluation of specific ultraviolet absorbance as an indicator of the chemical composition and reactivity of dissolved organic carbon, *Environ. Sci. Technol.*, 2003, **37**, 4702–4708.

72 A. M. Hansen, T. E. C. Kraus, B. A. Pellerin, J. A. Fleck, B. D. Downing and B. A. Bergamaschi, Optical properties of dissolved organic matter (DOM): Effects of biological and photolytic degradation, *Limnol. Oceanogr.*, 2016, **61**, 1015–1032.

73 F. J. Rodríguez, P. Schlenger and M. García-Valverde, Monitoring changes in the structure and properties of humic substances following ozonation using UV-Vis, FTIR and ^{1}H NMR techniques, *Sci. Total Environ.*, 2016, **541**, 623–637.

74 S. Chowdhury, Trihalomethanes in drinking water: Effect of natural organic matter distribution, *Water SA*, 2013, **39**, 1–8.

75 H. De Haan and T. De Boer, Applicability of Light Absorbance and Fluorescence as Measures of Concentration and Molecular Size of Dissolved Organic Carbon in Humic Lake Tjeukemeer, *Water Res.*, 1987, **21**, 731–734.

76 J. R. Helms, A. Stubbins, J. D. Ritchie, E. C. Minor, D. J. Kieber and K. Mopper, Absorption spectral slopes and slope ratios as indicators of molecular weight, source, and photobleaching of chromophoric dissolved organic matter, *Limnol. Oceanogr.*, 2008, **53**, 955–969.

77 A. T.-S. Chow, Y. Ulus, G. Huang, M. A. Kline and W.-Y. Cheah, Challenges in quantifying and

This journal is © The Royal Society of Chemistry 2025

Environ. Sci.: Processes Impacts, 2025, **27**, 2875–2893 | **2891**

characterizing dissolved organic carbon: Sampling, isolation, storage, and analysis, *J. Environ. Qual.*, 2022, **51**, 837–871.

78 M. S. Aulakh and D. A. Rennie, Azide Effects Upon N_2O Emission and Transformations of N in Soils, *Can. J. Soil Sci.*, 1985, **65**, 205–212.

79 D. Banerjee and H. W. Nesbitt, XPS study of dissolution of birnessite by humate with constraints on reaction mechanism, *Geochim. Cosmochim. Acta*, 2001, **65**, 1703–1714.

80 A. T. Stone, Microbial metabolites and the reductive dissolution of manganese oxides: Oxalate and pyruvate, *Geochim. Cosmochim. Acta*, 1987, **51**, 919–925.

81 S. P. Hansard, H. D. Easter and B. M. Voelker, Rapid reaction of nanomolar Mn(II) with superoxide radical in seawater and simulated freshwater, *Environ. Sci. Technol.*, 2011, **45**, 2811–2817.

82 I. G. McKendry, S. K. Kondaveeti, S. L. Shumlas, D. R. Strongin and M. J. Zdilla, Decoration of the layered manganese oxide birnessite with Mn(II/III) gives a new water oxidation catalyst with fifty-fold turnover number enhancement, *Dalton Trans.*, 2015, **44**, 12981–12984.

83 J. W. Stuckey, C. Goodwin, J. Wang, L. A. Kaplan, P. Vidal-Esquivel, T. P. Beebe Jr and D. L. Sparks, Impacts of hydrous manganese oxide on the retention and lability of dissolved organic matter, *Geochem. Trans.*, 2018, **19**, 6.

84 J. Chorover and M. K. Amistadi, Reaction of forest floor organic matter at goethite, birnessite and smectite surfaces, *Geochim. Cosmochim. Acta*, 2001, **65**, 95–109.

85 J. A. Greathouse, K. L. Johnson and H. C. Greenwell, Interaction of Natural Organic Matter with Layered Minerals: Recent Developments in Computational Methods at the Nanoscale, *Minerals*, 2014, **4**, 519–540.

86 S. Tu, G. J. Racz and T. B. Goh, Transformation of Synthetic Birnessite as Affected by pH and Manganese Concentration, *Clay Clay Miner.*, 1994, **42**, 321–330.

87 E. J. Elzinga, Reductive Transformation of Birnessite by Aqueous Mn(II), *Envrion. Sci. Technol.*, 2011, **45**, 6366–6372.

88 G. W. Luther, The Role of One- and Two-Electron Transfer Reactions in Forming Thermodynamically Unstable Intermediates as Barriers in Multi-Electron Redox Reactions, *Aquat. Geochem.*, 2010, **16**, 395–420.

89 J. A. Acosta, B. Jansen, K. Kalbitz, A. Faz and S. Martínez-Martínez, Salinity increases mobility of heavy metals in soils, *Chemosphere*, 2011, **85**, 1318–1324.

90 H. Cheng, J. Ma, J. Jiang, S.-Y. Pang, T. Yang and P. Wang, Aggregation Kinetics of Manganese Oxides Formed from permanganate activated by (Bi)sulfite: Dual Role of Ca^{2+} and $Mn^{II/III}$, *Water Res.*, 2019, **159**, 454–463.

91 J. J. Morgan and W. Stumm, Colloid-Chemical Properties of Manganese Dioxide, *J. Colloid Sci.*, 1964, **19**, 347–359.

92 J. W. Tonkin, L. S. Balistrieri and J. W. Murray, Modeling sorption of divalent metal cations on hydrous manganese oxide using the diffuse double layer model, *Appl. Geochem.*, 2004, **19**, 29–53.

93 H. S. Posselt, F. J. Aderson and W. J. Weber, Cation sorption on colloidal hydrous manganese dioxide, *Environ. Sci. Technol.*, 1968, **2**, 1087–1093.

94 A. G. Kalinichev, E. Iskrenova-Tchoukova, W.-Y. Ahn, M. M. Clark and R. J. Kirkpatrick, Effects of Ca^{2+} on supramolecular aggregation of natural organic matter in aqueous solutions: A comparison of molecular modeling approaches, *Geoderma*, 2011, **169**, 27–32.

95 E. Iskrenova-Tchoukova, A. G. Kalinichev and R. J. Kirkpatrick, Metal cation complexation with natural organic matter in aqueous solutions: molecular dynamics simulations and potentials of mean force, *Langmuir*, 2010, **26**, 15909–15919.

96 K. Hendrix, N. Bleyen, T. Mennecart, C. Bruggeman and E. Valcke, Sodium azide used as a microbial inhibitor caused unwanted by-products in anaerobic geochemical studies, *Appl. Geochem.*, 2019, **107**, 120–130.

97 E. L. Trainer, M. Ginder-Vogel and C. K. Remucal, Selective Reactivity and Oxidation of Dissolved Organic Matter by Manganese Oxides, *Environ. Sci. Technol.*, 2021, **55**, 12084–12094.

98 C. K. Remucal and M. Ginder-Vogel, A critical review of the reactivity of manganese oxides with organic contaminants, *Environ. Sci. Process Impacts*, 2014, **16**, 1247–1266.

99 K. Nambu and K. Yonebayashi, Acidic properties of dissolved organic matter leached from organic layers in temperate forests, *Soil Sci. Plant Nutr.*, 1999, **45**, 65–77.

100 S. Sagbas, C. Kantar and N. Sahiner, Preparation of Poly(Humic Acid) Particles and Their Use in Toxic Organo-Phenolic Compound Removal from Aqueous Environments, *Water, Air, Soil Pollut.*, 2013, **225**, 1809.

101 M. Zark and T. Dittmar, Universal molecular structures in natural dissolved organic matter, *Nat. Commun.*, 2018, **9**, 3178.

102 K. Johnson, G. Purvis, E. Lopez-Capel, C. Peacock, N. Gray, T. Wagner, C. März, L. Bowen, J. Ojeda, N. Finlay, S. Robertson, F. Worrall and C. Greenwell, Towards a mechanistic understanding of carbon stabilization in manganese oxides, *Nat. Commun.*, 2015, **6**, 7628.

103 Z. Ding, Y. Ding, F. Liu, J. Yang, R. Li, Z. Dang and Z. Shi, Coupled Sorption and Oxidation of Soil Dissolved Organic Matter on Manganese Oxides: Nano/Sub-nanoscale Distribution and Molecular Transformation, *Environ. Sci. Technol.*, 2022, **56**, 2783–2793.

104 S. Paul, T. Sharma, D. Saikia, P. P. Saikia, D. Borah and M. K. Baruah, Evaluation of pKa Values of Soil Humic Acids and their Complexation Properties, *Int. J. Plant Soil Sci.*, 2015, **6**, 218–228.

105 E. P. M. J. Fest, E. J. M. Temminghoff, R. N. J. Comans and W. H. van Riemsdijk, Partitioning of organic matter and heavy metals in a sandy soil: Effects of extracting solution, solid to liquid ratio and pH, *Geoderma*, 2008, **146**, 66–74.

106 A. T. Chow, K. K. Tanji and S. Gao, Production of dissolved organic carbon (DOC) and trihalomethane (THM) precursor from peat soils, *Water Res.*, 2003, **37**, 4475–4485.

2892 | *Environ. Sci.: Processes Impacts*, 2025, **27**, 2875–2893

This journal is © The Royal Society of Chemistry 2025

107 G. F. Koopmans and J. E. Groenenberg, Effects of soil oven-drying on concentrations and speciation of trace metals and dissolved organic matter in soil solution extracts of sandy soils, *Geoderma*, 2011, **161**, 147–158.

108 A. R. Schneider, M. Ponthieu, B. Cancès, A. Conreux, X. Morvan, M. Gommeaux, B. Marin and M. F. Benedetti, Influence of dissolved organic matter and manganese oxides on metal speciation in soil solution: A modelling approach, *Environ. Pollut.*, 2016, **213**, 618–627.

109 B. Kim, U. F. Lingappa, J. Magyar, D. Monteverde, J. S. Valentine, J. Cho and W. Fischer, Challenges of Measuring Soluble Mn(III) Species in Natural Samples, *Molecules*, 2022, **27**, 1661.

110 D. Kupka and P. Gruba, Effect of pH on the sorption of dissolved organic carbon derived from six tree species in forest soils, *Ecol. Indic.*, 2022, **140**, 108975.

This journal is © The Royal Society of Chemistry 2025

Environ. Sci.: Processes Impacts, 2025, **27**, 2875–2893 | **2893**